UNIVERSIDAD DE CONCEPCIÓN

Centro de Investigación en Ingeniería Matemática (CI^{2}MA)

A hybridizable discontinuous Galerkin method for the elasto–acoustic transmission problem

Gabriel N. Gatica, Salim Meddahi

PREPRINT 2026-20

SERIE DE PRE-PUBLICACIONES

A hybridizable discontinuous Galerkin method for the elasto–acoustic transmission problem

Gabriel N. Gatica and Salim Meddahi *

Abstract

We study a first-order velocity–stress–pressure formulation of the linear elasto-acoustic transmission problem, which couples elastodynamics in a solid subdomain with acoustic wave propagation in a compressible inviscid fluid. Unified Hilbert spaces are constructed to encode the transmission conditions within the operator domain. Casting the system as an abstract Cauchy problem, we verify the Lumer-Phillips conditions for the resulting block skew-symmetric operator and thereby establish existence, uniqueness, and energy stability of strong solutions via a contractive C_0-semigroup. We then develop a Hybridizable Discontinuous Galerkin (HDG) discretization of the semi-discrete system. A key feature of the method is a tailored penalization jump that permits free tangential slip on the acoustic side of the interface, consistent with the inviscid fluid model, while preserving the symmetry of the stabilization form. We prove consistency, stability, and optimal *hp*-convergence in the energy norm. Numerical experiments validate the theoretical predictions and confirm the robust performance of the method in both well-conditioned and stiff parameter settings relevant to practical applications, indicating in particular that the scheme is free of volumetric locking in the nearly incompressible regime.

MSC. 35L05, 35Q74, 74J05, 76Q05, 47D06.

Keywords. Elasto–acoustics, first-order hyperbolic systems, C_0-semigroups, well-posedness, hybridizable discontinuous Galerkin method, *hp*-convergence, fluid–solid coupling.

1 Introduction

Elasto-acoustic coupling across solid-fluid interfaces arises in seismic modelling, underwater acoustics, and biomedical ultrasound. The governing model couples linear elastodynamics in the solid with linear acoustics in a compressible inviscid fluid through transmission conditions enforcing continuity of normal velocity and balance of normal tractions at the interface. High-order spatial approximations are of particular importance in this setting: by dramatically reducing numerical dispersion and dissipation, they allow accurate simulations over extended frequency ranges and long time intervals, which is especially critical when multiple wave speeds coexist and contrasted material parameters challenge low-order schemes.

Several numerical frameworks have been extended to high-order formulations for elasto-acoustic problems, though each encounters characteristic limitations in coupled configurations; see [14] for a recent overview. Finite difference methods [19], despite their simplicity, suffer from geometric restrictions and accuracy loss at curved interfaces. High-order continuous finite elements [3] handle complex geometries naturally but are prone to spurious high-frequency modes that pollute the solution [11]. Spectral element methods [9] mitigate both dispersion errors and spurious modes through

*This research was supported by Ministerio de Ciencia e Innovación, Spain; by ANID-Chile through the project Centro de Modelamiento Matemático (FB210005); and by Centro de Investigación en Ingeniería Matemática (CI^{2}MA), Universidad de Concepción.

mass-lumped quadrature, but their efficiency relies critically on quadrilateral or hexahedral meshes, severely limiting geometric flexibility. Discontinuous Galerkin (DG) methods [1] offer the broadest geometric flexibility on general polyhedral meshes and support straightforward *hp*-adaptivity, but at a substantial computational cost: all element-interior degrees of freedom enter the global system, producing linear systems that are significantly larger and denser than those of conforming methods. This cost becomes particularly acute when implicit time integration is required, as in stiff or long-time regimes, and impedes the scalability of DG to large simulations.

Two high-order methods for the time-domain elasto-acoustic problem have been proposed recently. Terrana, Vilotte and Guillot [18] developed a spectral hybridizable discontinuous Galerkin method for elastic-acoustic wave propagation. Mottier, Ern, Khot and Guillot [14] proposed a Hybrid High-Order (HHO) method for the same coupled system in the first-order velocity–stress–pressure formulation, establishing energy-error estimates in the semi-discrete setting. The first-order-in-time formulation adopted in [18, 14] and in the present work simultaneously approximates primal and dual variables and is naturally compatible with a broad class of high-order implicit or explicit Runge–Kutta time integrators.

To achieve high-order accuracy on general meshes while controlling computational cost, we adopt the Hybridizable Discontinuous Galerkin (HDG) paradigm. Initially introduced by Cockburn, Gopalakrishnan and Lazarov [2], HDG provides a flexible and accurate framework for high-order finite element approximation on general meshes. HDG methods introduce trace unknowns on the mesh skeleton and eliminate element-interior degrees of freedom via static condensation, yielding a globally coupled system of skeleton unknowns comparable in size to that of conforming methods, while retaining the local conservation properties and *hp*-adaptivity of DG schemes. Furthermore, in the context of coupled wave physics, HDG methods provide a natural framework to weakly enforce transmission conditions. They have been successfully applied to acoustic and elastic wave equations [15, 4] and to fluid-structure interaction problems [17, 13]. In particular, the spectral HDG method of Terrana et al. [18] demonstrates the suitability of HDG for coupled elastic-acoustic simulation.

The HDG method developed here may be regarded as the elasto-acoustic counterpart of the FSI scheme recently analyzed in [13], where an incompressible viscous fluid (governed by the Stokes equations) is coupled with a linearly elastic solid. The present work replaces the viscous Stokes fluid with a compressible inviscid acoustic fluid, which fundamentally modifies the interface physics: whereas the Stokes–elastic model enforces full velocity continuity, the acoustic–elastic interface requires only continuity of the normal velocity component, allowing free tangential slip on the fluid side. This distinction is directly encoded at the discrete level through a tailored penalization jump operator that reduces to the normal component of the velocity difference on the acoustic side of the interface, thereby incorporating the inviscid slip condition into the stabilization form, while retaining a full vectorial jump in the elastic subdomain. The remaining discretization choices follow [13]: a velocity–stress formulation in the solid and a velocity–pressure formulation in the fluid, with polynomial degree $k \geq 0$ for stress and pressure and degree $k+1$ for velocities and their skeletal traces. Unlike the HDG approach of [18], which relies on upwind fluxes based on exact Riemann solvers, our stabilization is a symmetric penalty operator defined uniformly across the mesh. This choice enables a streamlined analysis: we establish existence, uniqueness, and energy stability of the continuous problem via the Lumer–Phillips theorem for C_0-semigroups, and prove optimal *hp*-error estimates for the semi-discrete HDG scheme in the energy norm. For the fully discrete scheme, we employ the second-order Crank–Nicolson method for transient simulations and L-stable SDIRK integrators for stiff parameter regimes; the latter are particularly relevant in the nearly incompressible limit, where the stress-based formulation also prevents volumetric locking [6]. The theoretical predictions are validated through *h*-, *p*-, and temporal convergence studies, and two Ricker wavelet benchmarks: an academic fluid–solid test against a semi-analytical solver and recent HHO results [14], and a physically realistic ocean–crust interface simulation with first-order absorbing boundary conditions, confirming robustness in

configurations relevant to underwater acoustics, seismic exploration, and medical ultrasound imaging.

The paper is organized as follows. Section 2 presents the elasto-acoustic model and its energy identity. Section 3 establishes well-posedness via the Lumer–Phillips theorem. Section 4 develops the HDG semi-discretization and its stability. Section 5 carries out the *hp*-convergence analysis. Section 6 reports the numerical experiments. Concluding remarks are collected in Section 7.

Notation and preliminaries

We denote the space of real matrices of order $d \times d$ by $\mathbb{M}$, and let

$$\mathbb{R}^{d\times d}_{\rm sym} := \{\boldsymbol{\tau} \in \mathbb{M};\ \boldsymbol{\tau} = \boldsymbol{\tau}^{\mathtt{t}}\}$$

be the subspace of symmetric matrices, where $\boldsymbol{\tau}^{\mathtt{t}} := (\tau_{ji})$ stands for the transpose of $\boldsymbol{\tau} = (\tau_{ij})$. The component-wise inner product of two matrices $\boldsymbol{\sigma}, \boldsymbol{\tau} \in \mathbb{M}$, called the Frobenius inner product, is defined by $\boldsymbol{\sigma} : \boldsymbol{\tau} := \sum_{i,j} \sigma_{ij}\tau_{ij}$. Let D be a polyhedral Lipschitz bounded domain of $\mathbb{R}^d$ ($d = 2, 3$), with boundary ∂D. Throughout this paper we apply all differential operators row-wise. Hence, given a tensorial function $\boldsymbol{\sigma} : D \to \mathbb{M}$ and a vector field $\boldsymbol{u} : D \to \mathbb{R}^d$, we define the divergence $\mathbf{div}\,\boldsymbol{\sigma} : D \to \mathbb{R}^d$, the gradient $\boldsymbol{\nabla u} : D \to \mathbb{M}$, and the linearized strain tensor (symmetric part of the gradient) $\boldsymbol{\varepsilon}(\boldsymbol{u}) : D \to \mathbb{R}^{d\times d}_{\rm sym}$ by

$$(\mathbf{div}\,\boldsymbol{\sigma})_i := \sum_j \partial_j \sigma_{ij}\,, \quad (\boldsymbol{\nabla u})_{ij} := \partial_j u_i\,, \quad \text{and} \quad \boldsymbol{\varepsilon}(\boldsymbol{u}) := \frac{1}{2}\left[\boldsymbol{\nabla u} + (\boldsymbol{\nabla u})^{\mathtt{t}}\right].$$

For $s \in \mathbb{R}$, $H^s(D, E)$ stands for the usual Hilbertian Sobolev space of functions with domain D and values in E, where E is either $\mathbb{R}$, $\mathbb{R}^d$, or $\mathbb{R}^{d\times d}_{\rm sym}$. In the case $E = \mathbb{R}$ we simply write $H^s(D)$. The norm of $H^s(D, E)$ is denoted $\|\cdot\|_{s,D}$ and the corresponding semi-norm $|\cdot|_{s,D}$, indistinctly for $E = \mathbb{R}, \mathbb{R}^d, \mathbb{R}^{d\times d}_{\rm sym}$. We use the convention $H^0(D, E) := L^2(D, E)$ and let $(\cdot,\cdot)_D$ denote the L^2 inner product in $L^2(D, E)$, interpreted component-wise for vector and tensor fields:

$$(\boldsymbol{u}, \boldsymbol{v})_D := \int_D \boldsymbol{u}\cdot\boldsymbol{v} \quad \forall \boldsymbol{u}, \boldsymbol{v} \in L^2(D, \mathbb{R}^d), \qquad (\boldsymbol{\sigma}, \boldsymbol{\tau})_D := \int_D \boldsymbol{\sigma} : \boldsymbol{\tau} \quad \forall \boldsymbol{\sigma}, \boldsymbol{\tau} \in L^2(D, \mathbb{R}^{d\times d}_{\rm sym}). \tag{1.1}$$

The space of tensors in $L^2(D, \mathbb{R}^{d\times d}_{\rm sym})$ with divergence in $L^2(D, \mathbb{R}^d)$ is denoted

$$H(\mathbf{div}, D, \mathbb{R}^{d\times d}_{\rm sym}) := \{\boldsymbol{\tau} \in L^2(D, \mathbb{R}^{d\times d}_{\rm sym}) : \mathbf{div}\,\boldsymbol{\tau} \in L^2(D, \mathbb{R}^d)\}\,,$$

equipped with the norm

$$\|\boldsymbol{\tau}\|^2_{H(\mathbf{div},D)} := \|\boldsymbol{\tau}\|^2_{0,D} + \|\mathbf{div}\,\boldsymbol{\tau}\|^2_{0,D}\,.$$

Similarly, for vector fields we define

$$H(\mathrm{div}, D) := \{\boldsymbol{v} \in L^2(D, \mathbb{R}^d) : \mathrm{div}\,\boldsymbol{v} \in L^2(D)\}$$

with analogous norm. The Green formula

$$(\boldsymbol{\tau}, \boldsymbol{\varepsilon}(\boldsymbol{v}))_D + (\mathbf{div}\,\boldsymbol{\tau}, \boldsymbol{v})_D = \int_{\partial D} \boldsymbol{\tau}\boldsymbol{n}\cdot\boldsymbol{v} \qquad \forall \boldsymbol{v} \in H^1(D, \mathbb{R}^d), \tag{1.2}$$

where $\boldsymbol{n}$ denotes the outward unit normal to ∂D, extends the normal trace operator $\boldsymbol{\tau} \to (\boldsymbol{\tau}|_{\partial D})\boldsymbol{n}$ to a linear continuous mapping $(\cdot|_{\partial D})\boldsymbol{n} : H(\mathbf{div}, D, \mathbb{R}^{d\times d}_{\rm sym}) \to H^{-1/2}(\partial D, \mathbb{R}^d)$, where $H^{-1/2}(\partial D, \mathbb{R}^d)$ is the dual of $H^{1/2}(\partial D, \mathbb{R}^d)$.

2 Model problem

We present the mathematical elasto–acoustic model, adopting a first-order velocity-stress formulation in the solid and a velocity-pressure formulation in the fluid. This choice naturally exposes the energy structure and facilitates the subsequent semigroup analysis. After stating the governing equations and boundary conditions, we derive a formal energy i dentity that guides the construction of appropriate function spaces in Section 3.

2.1 Governing equations

Let $\Omega \subset \mathbb{R}^d$ ($d \in \{2,3\}$) be a bounded Lipschitz domain partitioned into an elastic solid Ω_s and a compressible inviscid fluid Ω_a, with interface $\Sigma := \partial\Omega_s \cap \partial\Omega_a$. The exterior boundary $\partial\Omega$ is endowed with the outward unit normal vector $\boldsymbol{n}$. We define $\Gamma_s := \partial\Omega_s \cap \partial\Omega$ and $\Gamma_a := \partial\Omega_a \cap \partial\Omega$, and assume the disjoint decompositions $\Gamma_s = \Gamma_s^D \cup \Gamma_s^N$ and $\Gamma_a = \Gamma_a^D \cup \Gamma_a^N$ (see Figure 2.1 for an illustration of the model geometry). The material parameters are the densities $\rho_s, \rho_a > 0$, a symmetric uniformly positive definite elasticity tensor $\mathcal{C}$ in Ω_s, and the compressibility coefficient $c > 0$ in Ω_a.

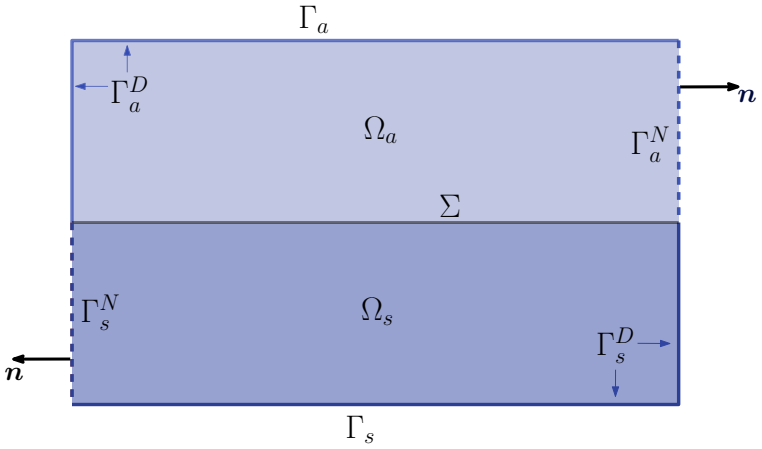

Figure 2.1: Illustration of the model geometry.

In the elastic domain Ω_s, we seek the velocity $\boldsymbol{u}_s : \Omega_s \times (0,T] \to \mathbb{R}^d$ and the Cauchy stress $\boldsymbol{\sigma} : \Omega_s \times (0,T] \to \mathbb{R}^{d\times d}_{\mathrm{sym}}$ satisfying:

$$\rho_s\, \dot{\boldsymbol{u}}_s - \mathbf{div}\, \boldsymbol{\sigma} = \boldsymbol{f} \qquad \text{in } \Omega_s \times (0,T], \tag{2.1a}$$

$$\dot{\boldsymbol{\sigma}} - \mathcal{C}\, \boldsymbol{\varepsilon}(\boldsymbol{u}_s) = \mathbf{0} \qquad \text{in } \Omega_s \times (0,T], \tag{2.1b}$$

where $\boldsymbol{f}$ represents body forces. These equations hold in $\Omega_s \times (0,T]$, representing the momentum balance and the elastic constitutive relation, respectively. On the external solid boundary, we impose homogeneous Dirichlet conditions on Γ_s^D (clamped) and homogeneous Neumann conditions on Γ_s^N (traction-free):

$$\boldsymbol{u}_s = \mathbf{0} \qquad \text{on } \Gamma_s^D \times (0,T], \tag{2.2a}$$

$$\boldsymbol{\sigma}\boldsymbol{n} = \mathbf{0} \qquad \text{on } \Gamma_s^N \times (0,T]. \tag{2.2b}$$

In turn, in Ω_a the unknowns are the velocity $\boldsymbol{u}_a$ and the pressure p. Conservation of momentum for

the inviscid fluid and linearized mass conservation read:

$$\rho_a \, \dot{\boldsymbol{u}}_a + \nabla p = \boldsymbol{0} \qquad \text{in } \Omega_a \times (0,T], \tag{2.3a}$$

$$c \, \dot{p} + \operatorname{div} \boldsymbol{u}_a = g \qquad \text{in } \Omega_a \times (0,T], \tag{2.3b}$$

where g is a given mass source. On the external acoustic boundary, we impose sound-soft and hard-wall conditions on Γ_a^D and Γ_a^N, respectively, i.e.,

$$p = 0 \qquad \text{on } \Gamma_a^D \times (0,T], \tag{2.4a}$$

$$\boldsymbol{u}_a \cdot \boldsymbol{n} = 0 \qquad \text{on } \Gamma_a^N \times (0,T]. \tag{2.4b}$$

The coupling across the interface Σ enforces traction balance and kinematic compatibility. Since the inviscid fluid exerts only a normal pressure force, and the normal component of velocity must be continuous, we impose

$$\boldsymbol{\sigma} \boldsymbol{n}_s = p \, \boldsymbol{n}_a \qquad \text{on } \Sigma \times (0,T], \tag{2.5a}$$

$$\boldsymbol{u}_s \cdot \boldsymbol{n}_s + \boldsymbol{u}_a \cdot \boldsymbol{n}_a = 0 \qquad \text{on } \Sigma \times (0,T], \tag{2.5b}$$

where $\boldsymbol{n}_s$ and $\boldsymbol{n}_a = -\boldsymbol{n}_s$ denote the outward unit normals to $\partial\Omega_s$ and $\partial\Omega_a$, respectively. The tangential component of the fluid velocity remains unconstrained, consistent with the slip condition for inviscid flow. To complete the initial-boundary value problem, we prescribe initial conditions at $t = 0$:

$$\boldsymbol{u}_s(0) = \boldsymbol{u}_s^0, \quad \boldsymbol{\sigma}(0) = \boldsymbol{\sigma}^0 \qquad \text{in } \Omega_s, \tag{2.6a}$$

$$\boldsymbol{u}_a(0) = \boldsymbol{u}_a^0, \quad p(0) = p^0 \qquad \text{in } \Omega_a, \tag{2.6b}$$

where typically $\boldsymbol{\sigma}^0 = \mathcal{C}\boldsymbol{\varepsilon}(\boldsymbol{d}^0)$ is determined from an initial displacement field $\boldsymbol{d}^0$.

3 Well-posedness

Formally multiplying the solid momentum equation by $\boldsymbol{u}_s$, the elastic constitutive law by $\mathcal{C}^{-1}\boldsymbol{\sigma}$, the fluid momentum equation by $\boldsymbol{u}_a$, and the mass balance by p, then integrating by parts over Ω_s and Ω_a respectively and exploiting the homogeneous boundary and transmission conditions, one arrives (in the source-free case) at the energy identity

$$\tfrac{1}{2} \, \tfrac{\mathrm{d}}{\mathrm{d}t} \Big(\|\rho_s^{1/2} \boldsymbol{u}_s\|_{0,\Omega_s}^2 + \|\mathcal{C}^{-1/2} \boldsymbol{\sigma}_s\|_{0,\Omega_s}^2 + \|\rho_a^{1/2} \boldsymbol{u}_a\|_{0,\Omega_a}^2 + \|c^{1/2} p\|_{0,\Omega_a}^2 \Big) = 0. \tag{3.1}$$

This energy suggests the natural norms for the problem: kinetic energies weighted by density and potential energies weighted by compliance. This section constructs unified Hilbert spaces for the coupled system and casts the transmission problem as an abstract evolution equation. By verifying the Lumer-Phillips conditions we prove that the evolution operator generates a contractive semigroup, thereby establishing existence, uniqueness, and stability.

To formulate the coupled problem abstractly, we unify the solid and fluid velocities into a single global field $\boldsymbol{u} : \Omega \to \mathbb{R}^d$ defined by $\boldsymbol{u}|_{\Omega_s} := \boldsymbol{u}_s$ and $\boldsymbol{u}|_{\Omega_a} := \boldsymbol{u}_a$. Letting $\rho : \Omega \to \mathbb{R}$ denote the piecewise-constant density (taking value ρ_s in Ω_s and ρ_a in Ω_a), we construct the velocity Hilbert space

$$\mathcal{H}^u := L^2(\Omega, \mathbb{R}^d) \tag{3.2}$$

equipped with the weighted inner product

$$(\boldsymbol{u},\boldsymbol{v})_{\mathcal{H}^u} := (\rho\boldsymbol{u},\boldsymbol{v})_\Omega, \quad \text{and induced norm} \quad \|\boldsymbol{v}\|^2_{\mathcal{H}^u} = \|\rho^{1/2}\boldsymbol{v}\|^2_{0,\Omega}\,.$$

For stress and pressure, we embed the fluid pressure as $-p\mathrm{I}_d$ within the symmetric tensor space and define the unified field $\boldsymbol{\sigma}_p : \Omega \times (0,T] \to \mathbb{R}^{d\times d}_{\mathrm{sym}}$ by

$$\boldsymbol{\sigma}_p := \begin{cases} \boldsymbol{\sigma} & \text{in } \Omega_s, \\ -p\,\mathrm{I}_d & \text{in } \Omega_a, \end{cases}$$

where I_d denotes the $d \times d$ identity matrix. We introduce the space

$$\mathcal{H}^\sigma := \{\boldsymbol{\tau}_q \in L^2(\Omega,\mathbb{R}^{d\times d}_{\mathrm{sym}}) :\ \boldsymbol{\tau}_q|_{\Omega_a} = -q\,\mathrm{I}_d \text{ for some } q \in L^2(\Omega_a)\} \tag{3.3}$$

equipped with the inner product

$$(\boldsymbol{\sigma}_p,\boldsymbol{\tau}_q)_{\mathcal{H}^\sigma} := (\mathcal{C}^{-1}\boldsymbol{\sigma},\boldsymbol{\tau})_{\Omega_s} + (cp,q)_{\Omega_a}\,.$$

We denote the corresponding norm $\|\boldsymbol{\tau}_q\|^2_{\mathcal{H}^\sigma} := (\boldsymbol{\tau}_q,\boldsymbol{\tau}_q)_{\mathcal{H}^\sigma}$. Owing to the normal-velocity transmission condition, the global velocity belongs to

$$\mathcal{X}^u := \big\{\, \boldsymbol{v} \in H(\mathrm{div},\Omega) \ :\ \boldsymbol{v}_s \in H^1(\Omega_s;\mathbb{R}^d),\ \text{with } \boldsymbol{v}_s|_{\Gamma^D_s} = \mathbf{0} \text{ and } (\boldsymbol{v}_a\cdot\boldsymbol{n})|_{\Gamma^N_a} = 0\,\big\}.$$

Similarly, the traction-balance condition ensures the continuity of the normal trace of $\boldsymbol{\sigma}_p$ across Σ, leading to the stress-pressure space

$$\mathcal{X}^\sigma := \Big\{\, \boldsymbol{\tau}_q \in H(\mathbf{div},\Omega;\mathbb{R}^{d\times d}_{\mathrm{sym}}) \cap \mathcal{H}^\sigma :\ \ \text{with } q \in H^1(\Omega_a),\ q|_{\Gamma^D_a} = 0,\ \text{and } (\boldsymbol{\tau}\boldsymbol{n})|_{\Gamma^N_s} = \mathbf{0}\,\Big\}.$$

With these definitions in hand, we introduce the linear operator $\mathcal{D} : \mathcal{X}^\sigma \subset \mathcal{H}^\sigma \to \mathcal{H}^u$ and its formal adjoint $\mathcal{D}^H : \mathcal{X}^u \subset \mathcal{H}^u \to \mathcal{H}^\sigma$ by

$$\mathcal{D}\,\boldsymbol{\tau}_q := -\rho^{-1}\,\mathbf{div}\,\boldsymbol{\tau}_q = \begin{cases} -\rho_s^{-1}\,\mathbf{div}\,\boldsymbol{\tau} & \text{in } \Omega_s, \\ \rho_a^{-1}\nabla q & \text{in } \Omega_a, \end{cases} \quad \text{and} \quad \mathcal{D}^H\boldsymbol{v} := \begin{cases} \mathcal{C}\boldsymbol{\varepsilon}(\boldsymbol{v}_s) & \text{in } \Omega_s, \\ c^{-1}\,\mathrm{div}(\boldsymbol{v}_a)\mathrm{I}_d & \text{in } \Omega_a. \end{cases}$$

By construction, the following Green's identity holds:

$$(\mathcal{D}\,\boldsymbol{\tau}_q,\boldsymbol{v})_{\mathcal{H}^u} = (\boldsymbol{\tau}_q,\mathcal{D}^H\boldsymbol{v})_{\mathcal{H}^\sigma} \quad \forall \boldsymbol{v} \in \mathcal{X}^u \quad \text{and} \quad \boldsymbol{\tau}_q \in \mathcal{X}^\sigma. \tag{3.4}$$

LEMMA 3.1. The operators $\mathcal{D} : \mathcal{X}^\sigma \subset \mathcal{H}^\sigma \to \mathcal{H}^u$ and $\mathcal{D}^H : \mathcal{X}^u \subset \mathcal{H}^u \to \mathcal{H}^\sigma$ are closed.

Proof. Closedness follows from convergence in graph norms and continuity of trace operators. We present the argument for $\mathcal{D}$; the proof for $\mathcal{D}^H$ follows a similar structure.

Step 1: Sequential convergence. Let $(\boldsymbol{\sigma}_{p,n})_{n\in\mathbb{N}} \subset \mathcal{X}^\sigma$ be such that $\boldsymbol{\sigma}_{p,n} \to \boldsymbol{\zeta}$ in $\mathcal{H}^\sigma$ and $\mathcal{D}\boldsymbol{\sigma}_{p,n} \to \boldsymbol{w}$ in $\mathcal{H}^u$. The two assumptions together control both $\boldsymbol{\sigma}_{p,n}$ in L^2 and $\mathbf{div}\,\boldsymbol{\sigma}_{p,n}$ in L^2, so the sequence is Cauchy in $H(\mathbf{div},\Omega;\mathbb{R}^{d\times d}_{\mathrm{sym}})$ and converges to $\boldsymbol{\zeta}$ in that space by completeness. Closedness of the distributional divergence then yields $\mathbf{div}\,\boldsymbol{\zeta} = \lim \mathbf{div}\,\boldsymbol{\sigma}_{p,n}$, hence $\mathcal{D}\boldsymbol{\zeta} = \boldsymbol{w}$.

Step 2: Preservation of structural constraints. It remains to verify $\boldsymbol{\zeta} \in \mathcal{X}^\sigma$, i.e., $\boldsymbol{\zeta}|_{\Omega_a} = -p\mathrm{I}_d$ for some $p \in H^1(\Omega_a)$ satisfying $p|_{\Gamma^D_a} = 0$, and $(\boldsymbol{\zeta}\boldsymbol{n})|_{\Gamma^N_s} = \mathbf{0}$. Since each $\boldsymbol{\sigma}_{p,n}$ has the form $-p_n\mathrm{I}_d$ in Ω_a, convergence in $L^2(\Omega_a,\mathbb{R}^{d\times d}_{\mathrm{sym}})$ yields $\boldsymbol{\zeta}|_{\Omega_a} = -p\mathrm{I}_d$ for some $p \in L^2(\Omega_a)$. The relation $\mathbf{div}\,\boldsymbol{\sigma}_{p,n}|_{\Omega_a} = -\nabla p_n \to \mathbf{div}\,\boldsymbol{\zeta}|_{\Omega_a}$ in $L^2(\Omega_a,\mathbb{R}^d)$ implies $p_n \to p$ in $H^1(\Omega_a)$. Continuity of the trace operator $H^1(\Omega_a) \to$

$L^2(\Gamma_a^D)$ then gives $p|_{\Gamma_a^D} = \lim p_n|_{\Gamma_a^D} = 0$. Similarly, $(\boldsymbol{\zeta}\boldsymbol{n})|_{\Gamma_s^N} = \lim(\boldsymbol{\sigma}_{p,n}\boldsymbol{n})|_{\Gamma_s^N} = \mathbf{0}$ by continuity of the trace $H(\mathbf{div}, \Omega_s; \mathbb{R}^{d\times d}_{\mathrm{sym}}) \to H^{-1/2}(\partial\Omega_s, \mathbb{R}^d)$. Therefore $\boldsymbol{\zeta} \in \mathcal{X}^\sigma$ and $\mathcal{D}$ is closed.

Closedness of $\mathcal{D}^H$: Consider a sequence $(\boldsymbol{u}_n)_{n\in\mathbb{N}} \subset \mathcal{X}^u$ such that $\boldsymbol{u}_n \to \boldsymbol{u}$ in $\mathcal{H}^u$ and $\mathcal{D}^H\boldsymbol{u}_n \to \boldsymbol{\zeta}$ in $\mathcal{H}^\sigma$. The convergence $\mathcal{D}^H\boldsymbol{u}_n \to \boldsymbol{\zeta}$ implies $\mathcal{C}\boldsymbol{\varepsilon}(\boldsymbol{u}_{s,n}) \to \boldsymbol{\zeta}|_{\Omega_s}$ in $L^2(\Omega_s, \mathbb{R}^{d\times d}_{\mathrm{sym}})$, so $\boldsymbol{\varepsilon}(\boldsymbol{u}_{s,n})$ converges in L^2. Combined with $\boldsymbol{u}_{s,n} \to \boldsymbol{u}_s$ in $L^2(\Omega_s, \mathbb{R}^d)$, Korn's inequality upgrades this to convergence in $H^1(\Omega_s, \mathbb{R}^d)$, giving $(\boldsymbol{u}_{s,n})_n$ Cauchy in $H^1(\Omega_s, \mathbb{R}^d)$ with limit $\boldsymbol{u}|_{\Omega_s} \in H^1(\Omega_s, \mathbb{R}^d)$. Similarly, $(\boldsymbol{u}_{a,n})_n := (\boldsymbol{u}_n|_{\Omega_a})_n$ is Cauchy in $H(\mathrm{div}, \Omega_a)$ with limit $\boldsymbol{u}|_{\Omega_a} \in H(\mathrm{div}, \Omega_a)$. This ensures $\mathcal{D}^H\boldsymbol{u} = \boldsymbol{\zeta}$. By continuity of trace operators and the constraints $(\boldsymbol{u}_{s,n}\cdot\boldsymbol{n}_s + \boldsymbol{u}_{a,n}\cdot\boldsymbol{n}_a)|_\Sigma = 0$, $\boldsymbol{u}_{s,n}|_{\Gamma_s^D} = \mathbf{0}$, and $(\boldsymbol{u}_{a,n}\cdot\boldsymbol{n})|_{\Gamma_a^N} = 0$ for all n, we deduce $\boldsymbol{u} \in H(\mathrm{div}, \Omega)$, $\boldsymbol{u}_s|_{\Gamma_s^D} = \mathbf{0}$, and $(\boldsymbol{u}_a\cdot\boldsymbol{n})|_{\Gamma_a^N} = 0$. Therefore $\boldsymbol{u} \in \mathcal{X}^u$, proving closedness of $\mathcal{D}^H$. □

Remark 3.1. Equipping $\mathcal{X}^\sigma$ and $\mathcal{X}^u$ with the graph inner products

$$(\boldsymbol{\sigma}_p, \boldsymbol{\tau}_q)_{\mathcal{X}^\sigma} := (\boldsymbol{\sigma}_p, \boldsymbol{\tau}_q)_{\mathcal{H}^\sigma} + (\mathcal{D}\boldsymbol{\sigma}_p, \mathcal{D}\boldsymbol{\tau}_q)_{\mathcal{H}^u} \quad \forall \boldsymbol{\sigma}_p, \boldsymbol{\tau}_q \in \mathcal{X}^\sigma,$$
$$(\boldsymbol{u}, \boldsymbol{v})_{\mathcal{X}^u} := (\boldsymbol{u}, \boldsymbol{v})_{\mathcal{H}^u} + (\mathcal{D}^H\boldsymbol{u}, \mathcal{D}^H\boldsymbol{v})_{\mathcal{H}^\sigma} \quad \forall \boldsymbol{u}, \boldsymbol{v} \in \mathcal{X}^u,$$

yields Hilbert spaces.

We introduce the linear operator $\mathbb{A} : \mathcal{D}(\mathbb{A}) \subset \mathcal{H}^u \times \mathcal{H}^\sigma \to \mathcal{H}^u \times \mathcal{H}^\sigma$ with domain $\mathcal{D}(\mathbb{A}) := \mathcal{X}^u \times \mathcal{X}^\sigma$ and such that

$$\mathbb{A}\begin{pmatrix}\boldsymbol{v}\\ \boldsymbol{\tau}_q\end{pmatrix} := \begin{pmatrix}\mathbf{0} & \mathcal{D}\\ -\mathcal{D}^H & \mathbf{0}\end{pmatrix}\begin{pmatrix}\boldsymbol{v}\\ \boldsymbol{\tau}_q\end{pmatrix}, \quad \forall (\boldsymbol{v}, \boldsymbol{\tau}_q) \in \mathcal{D}(\mathbb{A}).$$

Note that $\mathcal{D}(\mathbb{A}) = \mathcal{X}^u \times \mathcal{X}^\sigma$, so the domain of $\mathbb{A}$ consists precisely of those velocity-stress pairs satisfying the regularity and boundary conditions identified earlier. We can write equations (2.1)-(2.6) as the abstract Cauchy problem: find $(\boldsymbol{u}, \boldsymbol{\sigma}_p) \in \mathcal{H}^u \times \mathcal{H}^\sigma$ such that

$$\frac{\mathrm{d}}{\mathrm{d}t}\begin{pmatrix}\boldsymbol{u}\\ \boldsymbol{\sigma}_p\end{pmatrix} + \mathbb{A}\begin{pmatrix}\boldsymbol{u}\\ \boldsymbol{\sigma}_p\end{pmatrix} = \begin{pmatrix}\widetilde{\boldsymbol{f}}\\ \boldsymbol{G}\end{pmatrix}, \qquad (\boldsymbol{u}(0), \boldsymbol{\sigma}_p(0)) = (\boldsymbol{u}^0, \boldsymbol{\sigma}_p^0) \tag{3.5}$$

where $\boldsymbol{u}^0|_{\Omega_s} := \boldsymbol{u}_s^0$, $\boldsymbol{u}^0|_{\Omega_a} := \boldsymbol{u}_a^0$, $\boldsymbol{\sigma}_p^0|_{\Omega_s} := \boldsymbol{\sigma}^0$, and $\boldsymbol{\sigma}_p^0|_{\Omega_a} := -p^0\mathrm{I}_d$. Moreover, $\widetilde{\boldsymbol{f}} \in \mathcal{H}^u$ is defined by $\widetilde{\boldsymbol{f}}|_{\Omega_s} := {}^1\!/_{\rho_s}\boldsymbol{f}$ and $\widetilde{\boldsymbol{f}}|_{\Omega_a} := \mathbf{0}$, while $G \in \mathcal{H}^\sigma$ is given by $\boldsymbol{G}|_{\Omega_s} := \mathbf{0}$ and $\boldsymbol{G}|_{\Omega_a} := -\frac{1}{c}\,g\,\mathrm{I}_d$.

We now address the two conditions of the Lumer–Phillips theorem: monotonicity of $\mathbb{A}$ and surjectivity of $\mathbb{I} + \mathbb{A}$. For the first, the Green identity (3.4) gives, for all $(\boldsymbol{v}, \boldsymbol{\tau}_q) \in \mathcal{D}(\mathbb{A})$,

$$(\mathbb{A}(\boldsymbol{v}, \boldsymbol{\tau}_q), (\boldsymbol{v}, \boldsymbol{\tau}_q)) = (\mathcal{D}\boldsymbol{\tau}_q, \boldsymbol{v})_{\mathcal{H}^u} - (\mathcal{D}^H\,\boldsymbol{v}, \boldsymbol{\tau}_q)_{\mathcal{H}^\sigma} = 0 \quad \forall (\boldsymbol{v}, \boldsymbol{\tau}_q) \in \mathcal{D}(\mathbb{A}).$$

Denoting by $\mathbb{I}$ the identity operator in $\mathcal{H}^u \times \mathcal{H}^\sigma$, we now verify the range condition.

Lemma 3.2. The operator $\mathbb{I} + \mathbb{A} : \mathcal{D}(\mathbb{A}) \to \mathcal{H}^u \times \mathcal{H}^\sigma$ is surjective.

Proof. Given $(\boldsymbol{f}, G) \in \mathcal{H}^u \times \mathcal{H}^\sigma$, we need to find $(\boldsymbol{u}^*, \boldsymbol{\sigma}_p^*) \in \mathcal{X}^u \times \mathcal{X}^\sigma$ solving

$$\boldsymbol{u}^* + \mathcal{D}\boldsymbol{\sigma}_p^* = \boldsymbol{f}, \qquad \boldsymbol{\sigma}_p^* - \mathcal{D}^H\,\boldsymbol{u}^* = G.$$

Eliminating $\boldsymbol{\sigma}_p^*$, we deduce that $\boldsymbol{u}^* \in \mathcal{X}^u$ must solve the variational problem:

$$(\boldsymbol{u}^*, \boldsymbol{v})_{\mathcal{X}^u} = (\boldsymbol{f}, \boldsymbol{v})_{\mathcal{H}^u} - (G, \mathcal{D}^H\,\boldsymbol{v})_{\mathcal{H}^\sigma} \quad \forall \boldsymbol{v} \in \mathcal{X}^u.$$

The left-hand side of this equation is exactly the inner product on $\mathcal{X}^u$ and the right-hand side is a bounded linear functional by the Cauchy–Schwarz inequality: $|(\boldsymbol{f}, \boldsymbol{v})_{\mathcal{H}^u} - (G, \mathcal{D}^H\boldsymbol{v})_{\mathcal{H}^\sigma}| \le (\|\boldsymbol{f}\|_{\mathcal{H}^u} +$

$\|G\|_{\mathcal{H}^\sigma})\|\boldsymbol{v}\|_{\mathcal{X}^u}$. Thus, the Riesz representation theorem yields a unique solution $\boldsymbol{u}^* \in \mathcal{X}^u$ to this problem. We then define $\boldsymbol{\sigma}_p^* := G + \mathcal{D}^H \boldsymbol{u}^* \in \mathcal{H}^\sigma$. This immediately satisfies $\boldsymbol{\sigma}_p^* - \mathcal{D}^H \boldsymbol{u}^* = G$. It remains to show that $\boldsymbol{\sigma}_p^* \in \mathcal{X}^\sigma$ and $\boldsymbol{u}^* + \mathcal{D}\boldsymbol{\sigma}_p^* = \boldsymbol{f}$. Rearranging the variational formulation for $\boldsymbol{u}^*$, we have

$$(\boldsymbol{\sigma}_p^*, \mathcal{D}^H \boldsymbol{v})_{\mathcal{H}^\sigma} = (\boldsymbol{f} - \boldsymbol{u}^*, \boldsymbol{v})_{\mathcal{H}^u} \quad \forall \boldsymbol{v} \in \mathcal{X}^u.$$

By the definition of the adjoint operator, this identity means precisely that $\boldsymbol{\sigma}_p^*$ belongs to the domain of $\mathcal{D}$, i.e., $\boldsymbol{\sigma}_p^* \in \mathcal{X}^\sigma$, with $\mathcal{D}\boldsymbol{\sigma}_p^* = \boldsymbol{f} - \boldsymbol{u}^* \in \mathcal{H}^u$. This simultaneously shows that $\boldsymbol{u}^* + \mathcal{D}\boldsymbol{\sigma}_p^* = \boldsymbol{f}$. Hence $\mathbb{I} + \mathbb{A}$ is onto. □

THEOREM 3.1 (Well-posedness). For $\boldsymbol{f} \in \mathcal{C}^1_{[0,T]}(L^2(\Omega_s, \mathbb{R}^d))$, $g \in \mathcal{C}^1_{[0,T]}(L^2(\Omega_a))$, and $(\boldsymbol{u}^0, \boldsymbol{\sigma}_p^0) \in \mathcal{X}^u \times \mathcal{X}^\sigma$, the problem (3.5) admits a unique solution with

$$\boldsymbol{u} \in \mathcal{C}^1([0,T]; \mathcal{H}^u) \cap \mathcal{C}^0([0,T]; \mathcal{X}^u), \qquad \boldsymbol{\sigma}_p \in \mathcal{C}^1([0,T]; \mathcal{H}^\sigma) \cap \mathcal{C}^0([0,T]; \mathcal{X}^\sigma),$$

which satisfies the stability bound

$$\max_{t\in[0,T]} \|\boldsymbol{u}(t)\|_{\mathcal{H}^u} + \max_{t\in[0,T]} \|\boldsymbol{\sigma}_p(t)\|_{\mathcal{H}^\sigma} \le C \Big\{ \|(\boldsymbol{u}^0, \boldsymbol{\sigma}_p^0)\|_{\mathcal{H}^u \times \mathcal{H}^\sigma} + \max_{t\in[0,T]} \|\boldsymbol{f}(t)\|_{0,\Omega_s} + \max_{t\in[0,T]} \|g(t)\|_{0,\Omega_a} \Big\}.$$

Proof. Having established that $\mathbb{A}$ is monotone (via the Green identity (3.4)) and that $\mathbb{I}+\mathbb{A}$ is surjective (Lemma 3.2), the Lumer–Phillips theorem yields that $-\mathbb{A}$ generates a contraction semigroup on $\mathcal{H}^u \times \mathcal{H}^\sigma$. The stated regularity and stability then follow from standard semigroup theory (e.g., [5, Theorem 76.7]). □

We will use the following equivalent variational formulation of (3.5): find $\boldsymbol{u} \in \mathcal{C}^1([0,T]; \mathcal{H}^u) \cap \mathcal{C}^0([0,T]; \mathcal{X}^u)$ and $\boldsymbol{\sigma}_p \in \mathcal{C}^1([0,T]; \mathcal{H}^\sigma) \cap \mathcal{C}^0([0,T]; \mathcal{X}^\sigma)$ such that for all $\boldsymbol{v} \in \mathcal{X}^u$ and $\boldsymbol{\tau}_q \in \mathcal{X}^\sigma$,

$$(\dot{\boldsymbol{u}}, \boldsymbol{v})_{\mathcal{H}^u} - B(\boldsymbol{\sigma}_p, \boldsymbol{v}) = (\boldsymbol{f}, \boldsymbol{v}_s)_{\Omega_s}, \tag{3.6a}$$

$$(\dot{\boldsymbol{\sigma}}_p, \boldsymbol{\tau}_q)_{\mathcal{H}^\sigma} + B(\boldsymbol{\tau}_q, \boldsymbol{u}) = (g, q)_{\Omega_a}, \tag{3.6b}$$

where the bounded bilinear form $B : \mathcal{X}^\sigma \times \mathcal{X}^u \to \mathbb{R}$ is defined by $B(\boldsymbol{\tau}_q, \boldsymbol{v}) := (\mathbf{div}\, \boldsymbol{\tau}_q, \boldsymbol{v})_\Omega$.

4 The HDG method

We now introduce the HDG discretization of (3.6). The method introduces skeletal unknowns $\widehat{\boldsymbol{u}}_h$ on the mesh skeleton, enabling local element-wise elimination by static condensation while achieving optimal convergence rates. We begin by defining the discrete spaces and deriving key approximation properties. For notational simplicity we assume henceforth that $\Gamma_s^D = \Gamma_s$ and $\Gamma_a^D = \Gamma_a$; the extension to other boundary conditions is straightforward and is exercised in the numerical experiments of Section 6, which include pure Neumann data on Γ_s and Robin absorbing conditions.

4.1 Discrete framework

Let $\mathcal{T}_h = \{K\}$ be a shape-regular, conforming partition of $\bar{\Omega}$ into simplices (triangles if $d = 2$, tetrahedra if $d = 3$), where h_K denotes the diameter of element K and $h := \max_{K\in\mathcal{T}_h} h_K$. We assume that the mesh conforms to the partition $\Omega = \Omega_s \cup \Omega_a$, meaning that each element K lies entirely within either Ω_s or Ω_a. We denote by $\mathcal{T}_h^s$ and $\mathcal{T}_h^a$ the submeshes corresponding to the solid and acoustic regions, respectively. We define a closed subset $F \subset \overline{\Omega}$ to be an interior edge/face if it has a positive $(d-1)$-dimensional measure and we can express it as the intersection of the closures of two

distinct elements K and K', i.e., $F = \bar{K} \cap \bar{K}'$. On the other hand, a closed subset $F \subset \overline{\Omega}$ is a boundary edge/face if there exists $K \in \mathcal{T}_h$ such that F is an edge/face of K and $F = \bar{K} \cap \partial\Omega$. We consider the set $\mathcal{F}_h^0$ of interior edges/faces and the set $\mathcal{F}_h^\partial$ of boundary edges/faces and let $\mathcal{F}_h = \mathcal{F}_h^0 \cup \mathcal{F}_h^\partial$. We further decompose $\mathcal{F}_h^\partial = \mathcal{F}_h^s \cup \mathcal{F}_h^a$. We also single out the set of interface faces $\mathcal{F}_h^\Sigma := \{F \in \mathcal{F}_h^0 : \ F \subset \Sigma\}$. We denote by h_F the diameter of an edge/face $F \in \mathcal{F}_h$ and assume that $\mathcal{T}_h$ is locally quasi-uniform with constant $\gamma > 0$. This means that, for all h and all $K \in \mathcal{T}_h$, we have that

$$h_F \le h_K \le \gamma h_F \quad \forall F \in \mathcal{F}(K), \tag{4.1}$$

where $\mathcal{F}(K)$ represents the set of edges/faces composing the element $K \in \mathcal{T}_h$.

Let us now define the function spaces and inner products on the mesh partition that underlie the HDG discretization. For all $s \ge 0$, the broken Sobolev space with respect to the partition $\mathcal{T}_h$ of $\bar{\Omega}$ is defined as

$$H^s(\mathcal{T}_h, E) := \{\boldsymbol{v} \in L^2(\Omega, E) : \quad \boldsymbol{v}|_K \in H^s(K, E) \quad \forall K \in \mathcal{T}_h\}, \quad \text{for } E \in \{\mathbb{R}, \mathbb{R}^d, \mathbb{R}^{d\times d}_{\rm sym}\}.$$

Following the usual convention, we write $H^0(\mathcal{T}_h, E) = L^2(\mathcal{T}_h, E)$ and $H^s(\mathcal{T}_h, \mathbb{R}) = H^s(\mathcal{T}_h)$. We introduce the inner product

$$(\psi, \varphi)_{\mathcal{T}_h} := \sum_{K\in\mathcal{T}_h} (\psi, \varphi)_K \quad \forall \psi, \varphi \in L^2(\mathcal{T}_h, E), \quad E \in \{\mathbb{R}, \mathbb{R}^d, \mathbb{R}^{d\times d}_{\rm sym}\}$$

and write $\|\psi\|^2_{0,\mathcal{T}_h} := (\psi, \psi)_{\mathcal{T}_h}$. Accordingly, we let $\partial\mathcal{T}_h := \{\partial K;\ K \in \mathcal{T}_h\}$ be the set of all element boundaries and define $L^2(\partial\mathcal{T}_h, \mathbb{R}^d)$ as the space of vector-valued functions which are square-integrable on each $\partial K \in \partial\mathcal{T}_h$. We define

$$\langle \boldsymbol{u}, \boldsymbol{v}\rangle_{\partial\mathcal{T}_h} := \sum_{K\in\mathcal{T}_h} \int_{\partial K} \boldsymbol{u}\cdot\boldsymbol{v}, \quad \text{and} \quad \|\boldsymbol{v}\|^2_{0,\partial\mathcal{T}_h} := \langle \boldsymbol{v}, \boldsymbol{v}\rangle_{\partial\mathcal{T}_h} \quad \forall \boldsymbol{u}, \boldsymbol{v} \in L^2(\partial\mathcal{T}_h, \mathbb{R}^d),$$

where $\langle \boldsymbol{u}, \boldsymbol{v}\rangle_{\partial K} := \sum_{F\in\mathcal{F}(K)} \int_F \boldsymbol{u}\cdot\boldsymbol{v}$. Besides, we equip the space $L^2(\mathcal{F}_h, \mathbb{R}^d) := \prod_{F\in\mathcal{F}_h} L^2(F, \mathbb{R}^d)$ with the inner product

$$(\widehat{\boldsymbol{u}}, \widehat{\boldsymbol{v}})_{\mathcal{F}_h} := \sum_{F\in\mathcal{F}_h} \int_F \widehat{\boldsymbol{u}}\cdot\widehat{\boldsymbol{v}} \quad \forall \widehat{\boldsymbol{u}}, \widehat{\boldsymbol{v}} \in L^2(\mathcal{F}_h, \mathbb{R}^d),$$

and denote the corresponding norm $\|\widehat{\boldsymbol{v}}\|^2_{0,\mathcal{F}_h} := (\widehat{\boldsymbol{v}}, \widehat{\boldsymbol{v}})_{\mathcal{F}_h}$. Hereafter, $\mathcal{P}_m(D)$ is the space of polynomials of degree at most $m \ge 0$ on D if D is a triangle/tetrahedron, and the space of polynomials of degree at most m in each variable in D if D is a quadrilateral/parallelepiped. The space of E-valued functions with components in $\mathcal{P}_m(D)$ is denoted $\mathcal{P}_m(D, E)$ where E is either $\mathbb{R}^d$, or $\mathbb{R}^{d\times d}_{\rm sym}$. We introduce the space of piecewise-polynomial functions

$$\mathcal{P}_m(\mathcal{T}_h) := \{v \in L^2(\mathcal{T}_h) :\ v|_K \in \mathcal{P}_m(K),\ \forall K \in \mathcal{T}_h\}$$

with respect to the partition $\mathcal{T}_h$ and the space of piecewise-polynomial functions

$$\mathcal{P}_m(\mathcal{F}_h) := \{\phi \in L^2(\mathcal{F}_h) :\ \phi|_F \in \mathcal{P}_m(F),\ \forall F \in \mathcal{F}_h\}$$

with respect to the partition $\mathcal{F}_h$. The subspace of $L^2(\mathcal{T}_h, E)$ with components in $\mathcal{P}_m(\mathcal{T}_h)$ is denoted $\mathcal{P}_m(\mathcal{T}_h, E)$ for $E \in \{\mathbb{R}^d, \mathbb{R}^{d\times d}_{\rm sym}\}$. Likewise, $\mathcal{P}_m(\mathcal{F}_h, \mathbb{R}^d)$ stands for the subspace of $L^2(\mathcal{F}_h, \mathbb{R}^d)$ with

components in $\mathcal{P}_m(\mathcal{F}_h)$. We finally consider

$$\mathcal{P}_m(\partial\mathcal{T}_h,\mathbb{R}^d) := \Big\{\boldsymbol{v}\in L^2(\partial\mathcal{T}_h,\mathbb{R}^d);\ \boldsymbol{v}|_{\partial K}\in\mathcal{P}_m(\partial K,\mathbb{R}^d),\ \forall K\in\mathcal{T}_h\Big\},$$

where $\mathcal{P}_m(\partial K,\mathbb{R}^d) := \prod_{F\in\mathcal{F}(K)}\mathcal{P}_m(F,\mathbb{R}^d)$. It is important to keep in mind that, by definition, the functions in $L^2(\partial\mathcal{T}_h,\mathbb{R}^d)$ and $\mathcal{P}_m(\partial\mathcal{T}_h,\mathbb{R}^d)$ are multi-valued on every interior face F, whereas the functions in $L^2(\mathcal{F}_h,\mathbb{R}^d)$ and $\mathcal{P}_m(\mathcal{F}_h,\mathbb{R}^d)$ are single-valued on each face F.

We consider $\boldsymbol{n}\in\mathcal{P}_0(\partial\mathcal{T}_h,\mathbb{R}^d)$, where $\boldsymbol{n}|_{\partial K}=\boldsymbol{n}_K$ is the unit normal vector to ∂K oriented towards the exterior of K. Obviously, if $F=K\cap K'$ is an interior edge/face of $\mathcal{F}_h$, then $\boldsymbol{n}_K=-\boldsymbol{n}_{K'}$ on F. If $\boldsymbol{v}\in H^s(\mathcal{T}_h,\mathbb{R}^d)$ and $\boldsymbol{\tau}\in H^s(\mathcal{T}_h,\mathbb{R}^{d\times d}_{\rm sym})$, with $s>1/2$, the functions $\boldsymbol{v}|_{\partial\mathcal{T}_h}\in L^2(\partial\mathcal{T}_h,\mathbb{R}^d)$ and $(\boldsymbol{\tau}|_{\partial\mathcal{T}_h})\boldsymbol{n}\in L^2(\partial\mathcal{T}_h,\mathbb{R}^d)$ are meaningful by virtue of the trace theorem. For the same reason, if $\boldsymbol{v}\in H^1(\Omega,\mathbb{R}^d)$ $\boldsymbol{v}|_{\mathcal{F}_h}$ is well-defined in $L^2(\mathcal{F}_h,\mathbb{R}^d)$. We denote by $h_{\mathcal{F}}$ the element of $\mathcal{P}_0(\mathcal{F}_h)$ given by $h_{\mathcal{F}}|_F := h_F$ for all $F\in\mathcal{F}_h$.

4.2 HDG discrete spaces

For a fixed polynomial degree $k\geq 0$, we define the discrete spaces for the stress-pressure field, velocity field, and the facet unknown. The stress-pressure space reflects the block structure of the problem: in the solid region the stress tensor is symmetric, while in the acoustic region it reduces to a spherical tensor $-q\mathrm{I}_d$. We set

$$\mathcal{H}_h^\sigma := \{\boldsymbol{\tau}_q\in\mathcal{P}_k(\mathcal{T}_h,\mathbb{R}^{d\times d}_{\rm sym}):\ \boldsymbol{\tau}_q|_{\Omega_a}=-q\mathrm{I}_d\},$$

approximating the continuous space $\mathcal{H}^\sigma$ defined in (3.3). The velocity is approximated one degree higher,

$$\mathcal{H}_h^u := \mathcal{P}_{k+1}(\mathcal{T}_h,\mathbb{R}^d),$$

consistently with the continuous space $\mathcal{H}^u$ of (3.2). Finally, HDG introduces a skeletal unknown $\widehat{\boldsymbol{u}}_h$ on the mesh skeleton, serving as the trace of the velocity on element faces. The corresponding facet space is

$$\mathcal{M}_h := \{\widehat{\boldsymbol{v}}\in\mathcal{P}_{k+1}(\mathcal{F}_h,\mathbb{R}^d):\ \widehat{\boldsymbol{v}}|_F=\boldsymbol{0}\text{ for all }F\in\mathcal{F}_h^s\}.$$

REMARK 4.1 (Full vector vs. normal-only facet unknowns). The facet space $\mathcal{M}_h$ employs full vector degrees of freedom on all faces except the solid Dirichlet boundary Γ_s. An alternative design would restrict $\widehat{\boldsymbol{u}}_h$ to normal components on acoustic faces and the interface, since the acoustic equations couple only the normal velocity. Our choice of full vector unknowns simplifies the implementation by avoiding face-orientation dependencies, at the cost of a slight increase in the number of degrees of freedom.

Since the interface condition (2.5b) couples only the normal component of the velocity across Σ (the inviscid fluid admits free tangential slip), we define the *penalization jump* $\boldsymbol{\delta}_h(\boldsymbol{v},\widehat{\boldsymbol{v}})\in L^2(\partial\mathcal{T}_h,\mathbb{R}^d)$ for $(\boldsymbol{v},\widehat{\boldsymbol{v}})\in H^1(\mathcal{T}_h,\mathbb{R}^d)\times L^2(\mathcal{F}_h,\mathbb{R}^d)$ by

$$\boldsymbol{\delta}_h(\boldsymbol{v},\widehat{\boldsymbol{v}})\big|_{\partial K} := \begin{cases}\boldsymbol{v}-\widehat{\boldsymbol{v}} & \text{for } K\in\mathcal{T}_h^s,\\ \boldsymbol{v}-\widehat{\boldsymbol{v}} & \text{on } \partial K\setminus\Sigma \text{ for } K\in\mathcal{T}_h^a,\\ \big((\boldsymbol{v}-\widehat{\boldsymbol{v}})\cdot\boldsymbol{n}\big)\boldsymbol{n} & \text{on } \partial K\cap\Sigma \text{ for } K\in\mathcal{T}_h^a,\end{cases} \tag{4.2}$$

where $\boldsymbol{n}$ denotes the outward unit normal to ∂K. The HDG semi-discrete problem seeks approximations $\boldsymbol{\sigma}_{p,h}\in\mathcal{C}^1([0,T];\mathcal{H}_h^\sigma)$, $\boldsymbol{u}_h\in\mathcal{C}^1([0,T];\mathcal{H}_h^u)$ and $\widehat{\boldsymbol{u}}_h\in\mathcal{C}^1([0,T];\mathcal{M}_h)$ such that, for all $(\boldsymbol{v},\widehat{\boldsymbol{v}})\in$

$\mathcal{H}_h^u \times \mathcal{M}_h$ and all $\boldsymbol{\tau}_q \in \mathcal{H}_h^\sigma$,

$$(\dot{\boldsymbol{u}}_h, \boldsymbol{v})_{\mathcal{H}^u} - B_h(\boldsymbol{\sigma}_{p,h}, (\boldsymbol{v}, \widehat{\boldsymbol{v}})) + \langle \tfrac{(k+1)^2}{h_{\mathcal{F}}} \boldsymbol{\delta}_h(\boldsymbol{u}_h, \widehat{\boldsymbol{u}}_h), \boldsymbol{\delta}_h(\boldsymbol{v}, \widehat{\boldsymbol{v}}) \rangle_{\partial \mathcal{T}_h} = (\boldsymbol{f}, \boldsymbol{v})_{\Omega_s}, \tag{4.3a}$$

$$(\dot{\boldsymbol{\sigma}}_{p,h}, \boldsymbol{\tau}_q)_{\mathcal{H}^\sigma} + B_h(\boldsymbol{\tau}_q, (\boldsymbol{u}_h, \widehat{\boldsymbol{u}}_h)) = (g, q)_{\Omega_a}, \tag{4.3b}$$

where

$$B_h(\boldsymbol{\tau}_q, (\boldsymbol{v}, \widehat{\boldsymbol{v}})) := -(\boldsymbol{\tau}_q, \boldsymbol{\varepsilon}(\boldsymbol{v}))_{\mathcal{T}_h} + \langle \boldsymbol{\tau}_q \boldsymbol{n}, \boldsymbol{v} - \widehat{\boldsymbol{v}} \rangle_{\partial \mathcal{T}_h}.$$

For the stability and convergence analysis, we endow the product space $H^1(\mathcal{T}_h, \mathbb{R}^d) \times L^2(\mathcal{F}_h, \mathbb{R}^d)$ with the semi-norm

$$|(\boldsymbol{v}, \widehat{\boldsymbol{v}})|_{1,h}^2 := \|\nabla \boldsymbol{v}\|_{0,\mathcal{T}_h}^2 + \left\| \tfrac{k+1}{h_{\mathcal{F}}^{1/2}} \boldsymbol{\delta}_h(\boldsymbol{v}, \widehat{\boldsymbol{v}}) \right\|_{0,\partial \mathcal{T}_h}^2 \quad \forall (\boldsymbol{v}, \widehat{\boldsymbol{v}}) \in H^1(\mathcal{T}_h, \mathbb{R}^d) \times L^2(\mathcal{F}_h, \mathbb{R}^d). \tag{4.4}$$

The following boundedness result for the bilinear form B_h is essential for the stability analysis.

LEMMA 4.1 (Boundedness of B_h). There exists a constant $C > 0$ independent of h, k, and the material parameters such that

$$|B_h(\boldsymbol{\tau}_q, (\boldsymbol{v}, \widehat{\boldsymbol{v}}))| \le C \|\boldsymbol{\tau}_q\|_{\mathcal{H}^\sigma} |(\boldsymbol{v}, \widehat{\boldsymbol{v}})|_{1,h} \quad \forall \boldsymbol{\tau}_q \in \mathcal{H}_h^\sigma,\ \forall (\boldsymbol{v}, \widehat{\boldsymbol{v}}) \in H^1(\mathcal{T}_h, \mathbb{R}^d) \times L^2(\mathcal{F}_h, \mathbb{R}^d). \tag{4.5}$$

Proof. The proof applies the Cauchy–Schwarz inequality to the broken inner products in B_h, then employs a discrete trace inequality to control boundary terms. By the definition of B_h and the Cauchy–Schwarz inequality, we have the estimate

$$|B_h(\boldsymbol{\tau}_q, (\boldsymbol{v}, \widehat{\boldsymbol{v}}))| \le \|\boldsymbol{\tau}_q\|_{0,\mathcal{T}_h} \|\nabla \boldsymbol{v}\|_{0,\mathcal{T}_h} + \|\tfrac{h_F^{1/2}}{k+1} \boldsymbol{\tau}_q \boldsymbol{n}\|_{0,\partial \mathcal{T}_h} \|\tfrac{k+1}{h_{\mathcal{F}}^{1/2}} \boldsymbol{\delta}_h(\boldsymbol{v}, \widehat{\boldsymbol{v}})\|_{0,\partial \mathcal{T}_h},$$

for all $\boldsymbol{\tau}_q \in \mathcal{H}_h^\sigma$ and $(\boldsymbol{v}, \widehat{\boldsymbol{v}}) \in H^1(\mathcal{T}_h, \mathbb{R}^d) \times L^2(\mathcal{F}_h, \mathbb{R}^d)$. The second term uses $\boldsymbol{\delta}_h$ rather than $\boldsymbol{v} - \widehat{\boldsymbol{v}}$ because $\boldsymbol{\tau}_q \boldsymbol{n}$ is purely normal on acoustic element faces (where $\boldsymbol{\tau}_q|_{\Omega_a} = -q \mathrm{I}_d$ implies $\boldsymbol{\tau}_q \boldsymbol{n} = -q \boldsymbol{n}$), so the dot product $\boldsymbol{\tau}_q \boldsymbol{n} \cdot (\boldsymbol{v} - \widehat{\boldsymbol{v}})$ depends only on the normal component $\boldsymbol{\delta}_h(\boldsymbol{v}, \widehat{\boldsymbol{v}}) \cdot \boldsymbol{n}$ on acoustic interface faces. If $\boldsymbol{\tau}_q \in \mathcal{P}_k(\mathcal{T}_h, \mathbb{R}_{\mathrm{sym}}^{d \times d})$, we can apply the discrete trace inequality (A.1) to obtain

$$\left\| \tfrac{h_F^{1/2}}{k+1} \boldsymbol{\tau}_q \boldsymbol{n} \right\|_{0,\partial \mathcal{T}_h} \le c \|\boldsymbol{\tau}_q\|_{0,\mathcal{T}_h},$$

and the result follows. □

5 Convergence analysis

We now prove optimal convergence of the HDG semidiscrete scheme. The argument proceeds in three steps: establishing consistency of the method with the continuous problem, deriving stability estimates for the discrete solution in terms of data, and combining these via projection error bounds to obtain *hp*-convergence rates.

5.1 Well-posedness and consistency of the semi-discrete problem

PROPOSITION 5.1. Problem (4.3) admits a unique solution.

Proof. The proof proceeds by eliminating the facet unknown $\widehat{\boldsymbol{u}}_h$ through static condensation, reducing

the problem to a finite-dimensional system of ODEs in $\mathcal{H}_h^u \times \mathcal{H}_h^\sigma$, for which existence and uniqueness follow from standard ODE theory. We can write the system (4.3) as the algebraic differential equation

$$\begin{aligned}
(\dot{\boldsymbol{u}}_h, \boldsymbol{v})_{\mathcal{H}^u} + (\boldsymbol{\sigma}_{p,h}, \boldsymbol{\varepsilon}(\boldsymbol{v}))_{\mathcal{T}_h} - \langle \boldsymbol{\sigma}_{p,h}\boldsymbol{n}, \boldsymbol{v}\rangle_{\partial\mathcal{T}_h} + \langle \tfrac{(k+1)^2}{h_{\mathcal{F}}}\boldsymbol{\delta}_h(\boldsymbol{u}_h, \widehat{\boldsymbol{u}}_h), \boldsymbol{\delta}_h(\boldsymbol{v}, \boldsymbol{0})\rangle_{\partial\mathcal{T}_h} &= (\boldsymbol{f}, \boldsymbol{v})_{\Omega_s}, \\
(\dot{\boldsymbol{\sigma}}_{p,h}, \boldsymbol{\tau}_q)_{\mathcal{H}^\sigma} - (\boldsymbol{\tau}_q, \boldsymbol{\varepsilon}(\boldsymbol{u}_h))_{\mathcal{T}_h} + \langle \boldsymbol{\tau}_q\boldsymbol{n}, \boldsymbol{u}_h - \widehat{\boldsymbol{u}}_h\rangle_{\partial\mathcal{T}_h} &= (g, q)_{\Omega_a}, \\
\langle \boldsymbol{\sigma}_{p,h}\boldsymbol{n}, \widehat{\boldsymbol{v}}\rangle_{\partial\mathcal{T}_h} + \langle \tfrac{(k+1)^2}{h_{\mathcal{F}}}\boldsymbol{\delta}_h(\boldsymbol{u}_h, \widehat{\boldsymbol{u}}_h), \boldsymbol{\delta}_h(\boldsymbol{0}, \widehat{\boldsymbol{v}})\rangle_{\partial\mathcal{T}_h} &= 0,
\end{aligned} \tag{5.1}$$

for all $\boldsymbol{v} \in \mathcal{H}_h^u$, $\boldsymbol{\tau}_q \in \mathcal{H}_h^\sigma$, and $\widehat{\boldsymbol{v}} \in \mathcal{M}_h$, where the third equation follows from testing (4.3a) with $(\boldsymbol{0}, \widehat{\boldsymbol{v}})$. From the third equation of (5.1), we can express the facet unknown $\widehat{\boldsymbol{u}}_h(t)$ for all $t \in (0, T]$ as follows:

$$\widehat{\boldsymbol{u}}_h|_F = \begin{cases}
\{\boldsymbol{u}_h\}|_F - \dfrac{h_F}{(k+1)^2}\{\boldsymbol{\sigma}_{p,h}\boldsymbol{n}\}|_F & \text{for } F \in \mathcal{F}_h^0 \setminus \mathcal{F}_h^\Sigma, \\
\widehat{\boldsymbol{u}}_h \cdot \boldsymbol{n}_s = \{\boldsymbol{u}_h\} \cdot \boldsymbol{n}_s - \dfrac{h_F}{(k+1)^2}\{\boldsymbol{\sigma}_{p,h}\boldsymbol{n}\} \cdot \boldsymbol{n}_s, & \\
(\mathrm{I}_d - \boldsymbol{n}_s\boldsymbol{n}_s^\top)\widehat{\boldsymbol{u}}_h = (\mathrm{I}_d - \boldsymbol{n}_s\boldsymbol{n}_s^\top)\Big(\boldsymbol{u}_h|_{K_s} - \dfrac{h_F}{(k+1)^2}\boldsymbol{\sigma}_{p,h}|_{K_s}\boldsymbol{n}_s\Big) & \text{for } F \in \mathcal{F}_h^\Sigma, \\
\boldsymbol{u}_h|_F - \dfrac{h_F}{(k+1)^2}(\boldsymbol{\sigma}_{p,h}\boldsymbol{n})|_F & \text{for } F \in \mathcal{F}_h^a, \\
\boldsymbol{0} & \text{for } F \in \mathcal{F}_h^s,
\end{cases} \tag{5.2}$$

where $\{\boldsymbol{u}_h\}|_F := \frac{1}{2}(\boldsymbol{u}_h|_K + \boldsymbol{u}_h|_{K'})|_F$ and $\{\boldsymbol{\sigma}_{p,h}\boldsymbol{n}\}|_F := \frac{1}{2}(\boldsymbol{\sigma}_{p,h}|_K\boldsymbol{n}_K + \boldsymbol{\sigma}_{p,h}|_{K'}\boldsymbol{n}_{K'})|_F$ for interior faces $F = \partial K \cap \partial K'$. In the interface case, $K_s \in \mathcal{T}_h^s$ and $K_a \in \mathcal{T}_h^a$ denote the solid and acoustic elements sharing F, and $\boldsymbol{n}_s := \boldsymbol{n}_{K_s}|_F$ is the outward unit normal from K_s on F. On interface faces $F \in \mathcal{F}_h^\Sigma$, the normal component of $\widehat{\boldsymbol{u}}_h$ follows the standard two-sided average (as for interior faces), while the tangential component is determined entirely by the solid side, reflecting the normal-only penalization of $\boldsymbol{\delta}_h$ on acoustic interface faces. Note that both formulas in the interface case are independent of the sign of $\boldsymbol{n}_s$: $(\mathrm{I}_d - \boldsymbol{n}_s\boldsymbol{n}_s^\top)$ is sign-invariant, and flipping $\boldsymbol{n}_s$ negates both sides of the normal-component equation simultaneously. The fourth case corresponds to the homogeneous Dirichlet boundary condition on Γ_s, which is enforced strongly through the definition of $\mathcal{M}_h$.

Substituting (5.2) into the first two equations of (5.1) eliminates $\widehat{\boldsymbol{u}}_h$ and yields a system of ordinary differential equations in the finite-dimensional spaces $\mathcal{H}_h^\sigma$ and $\mathcal{H}_h^u$:

$$\begin{aligned}
(\dot{\boldsymbol{u}}_h, \boldsymbol{v})_{\mathcal{H}^u} + (\boldsymbol{\sigma}_{p,h}, \boldsymbol{\varepsilon}(\boldsymbol{v}))_{\mathcal{T}_h} - \langle \boldsymbol{\sigma}_{p,h}\boldsymbol{n}, \boldsymbol{v}\rangle_{\partial\mathcal{T}_h} + \langle \tfrac{(k+1)^2}{h_{\mathcal{F}}}\boldsymbol{\delta}_h(\boldsymbol{u}_h, \widehat{\boldsymbol{u}}_h[\boldsymbol{u}_h, \boldsymbol{\sigma}_{p,h}]), \boldsymbol{\delta}_h(\boldsymbol{v}, \boldsymbol{0})\rangle_{\partial\mathcal{T}_h} &= (\boldsymbol{f}, \boldsymbol{v})_{\Omega_s}, \\
(\dot{\boldsymbol{\sigma}}_{p,h}, \boldsymbol{\tau}_q)_{\mathcal{H}^\sigma} - (\boldsymbol{\tau}_q, \boldsymbol{\varepsilon}(\boldsymbol{u}_h))_{\mathcal{T}_h} + \langle \boldsymbol{\tau}_q\boldsymbol{n}, \boldsymbol{u}_h - \widehat{\boldsymbol{u}}_h[\boldsymbol{u}_h, \boldsymbol{\sigma}_{p,h}]\rangle_{\partial\mathcal{T}_h} &= (g, q)_{\Omega_a},
\end{aligned} \tag{5.3}$$

where $\widehat{\boldsymbol{u}}_h[\boldsymbol{u}_h, \boldsymbol{\sigma}_{p,h}]$ denotes the facet unknown expressed in terms of $\boldsymbol{u}_h$ and $\boldsymbol{\sigma}_{p,h}$ via (5.2). We observe that $(\cdot,\cdot)_{\mathcal{H}^u}$ and $(\cdot,\cdot)_{\mathcal{H}^\sigma}$ are inner products on the finite-dimensional spaces $\mathcal{H}_h^u$ and $\mathcal{H}_h^\sigma$, respectively. By selecting suitable basis functions for these spaces, we can represent the semidiscrete problem (5.3) as a conventional first-order system of differential equations. Existence and uniqueness of the solution to (4.3) then follow from standard ODE theory. □

PROPOSITION 5.2 (Consistency). Assume the exact solution $(\boldsymbol{u}, \boldsymbol{\sigma}_p)$ of (3.6) has the additional regularity $\boldsymbol{u} \in \mathcal{C}^1([0,T]; H^1(\Omega, \mathbb{R}^d))$ and $\boldsymbol{\sigma}_p \in \mathcal{C}^1([0,T]; H^1(\mathcal{T}_h, \mathbb{R}^{d\times d}_{\mathrm{sym}}))$. Then the HDG scheme (4.3) is

consistent: for all $(\boldsymbol{v},\widehat{\boldsymbol{v}}) \in \mathcal{H}_h^u \times \mathcal{M}_h$ and $\boldsymbol{\tau}_q \in \mathcal{H}_h^\sigma$:

$$(\dot{\boldsymbol{u}},\boldsymbol{v})_{\mathcal{H}^u} - B_h(\boldsymbol{\sigma}_p,(\boldsymbol{v},\widehat{\boldsymbol{v}})) + \langle \tfrac{(k+1)^2}{h_{\mathcal{F}}}\boldsymbol{\delta}_h(\boldsymbol{u},\widehat{\boldsymbol{u}}),\boldsymbol{\delta}_h(\boldsymbol{v},\widehat{\boldsymbol{v}})\rangle_{\partial\mathcal{T}_h} = (\boldsymbol{f},\boldsymbol{v})_{\Omega_s},$$
$$(\dot{\boldsymbol{\sigma}}_p,\boldsymbol{\tau}_q)_{\mathcal{H}^\sigma} + B_h(\boldsymbol{\tau}_q,(\boldsymbol{u},\widehat{\boldsymbol{u}})) = (g,q)_{\Omega_a},$$

where $\widehat{\boldsymbol{u}} := \boldsymbol{u}|_{\mathcal{F}_h}$ denotes the trace of the exact velocity on the mesh skeleton.

Proof. The proof relies on three key observations.

Step 1: The stabilization term vanishes. Since $\boldsymbol{u} \in H^1(\Omega,\mathbb{R}^d)$ is continuous across inter-element boundaries, its trace $\widehat{\boldsymbol{u}} = \boldsymbol{u}|_{\mathcal{F}_h}$ is single-valued on each face. Consequently, $\boldsymbol{u}|_{\partial K} - \widehat{\boldsymbol{u}}|_{\partial K} = \boldsymbol{0}$ for all $K \in \mathcal{T}_h$, so $\boldsymbol{\delta}_h(\boldsymbol{u},\widehat{\boldsymbol{u}}) = \boldsymbol{0}$ (regardless of the case in (4.2)), and the stabilization term vanishes:

$$\langle \tfrac{(k+1)^2}{h_{\mathcal{F}}}\boldsymbol{\delta}_h(\boldsymbol{u},\widehat{\boldsymbol{u}}),\boldsymbol{\delta}_h(\boldsymbol{v},\widehat{\boldsymbol{v}})\rangle_{\partial\mathcal{T}_h} = 0.$$

Step 2: Relating B_h to B via integration by parts. For any $\boldsymbol{\tau}_q \in H^1(\mathcal{T}_h,\mathbb{R}^{d\times d}_{\mathrm{sym}})$ and $(\boldsymbol{v},\widehat{\boldsymbol{v}}) \in \mathcal{H}_h^u \times \mathcal{M}_h$, integration by parts on each element K yields

$$(\boldsymbol{\tau}_q,\boldsymbol{\varepsilon}(\boldsymbol{v}))_K = -(\mathbf{div}\,\boldsymbol{\tau}_q,\boldsymbol{v})_K + \langle \boldsymbol{\tau}_q\boldsymbol{n}_K,\boldsymbol{v}\rangle_{\partial K}.$$

Summing over all elements and substituting into the definition of B_h:

$$B_h(\boldsymbol{\tau}_q,(\boldsymbol{v},\widehat{\boldsymbol{v}})) = (\mathbf{div}\,\boldsymbol{\tau}_q,\boldsymbol{v})_{\mathcal{T}_h} - \langle \boldsymbol{\tau}_q\boldsymbol{n},\widehat{\boldsymbol{v}}\rangle_{\partial\mathcal{T}_h}. \tag{5.4}$$

Step 3: Boundary and interface contributions vanish. We now show that $\langle \boldsymbol{\sigma}_p\boldsymbol{n},\widehat{\boldsymbol{v}}\rangle_{\partial\mathcal{T}_h} = 0$ by examining interior and boundary contributions separately. On each interior face $F = \partial K \cap \partial K'$, since $\widehat{\boldsymbol{v}}$ is single-valued on F, the combined contribution is $(\boldsymbol{\sigma}_p|_K\boldsymbol{n}_K + \boldsymbol{\sigma}_p|_{K'}\boldsymbol{n}_{K'})\cdot\widehat{\boldsymbol{v}}|_F$. Since $\boldsymbol{\sigma}_p \in \mathcal{X}^\sigma \subset H(\mathrm{div},\Omega,\mathbb{R}^{d\times d}_{\mathrm{sym}})$, the normal-traction jump vanishes across every interior face:

$$\boldsymbol{\sigma}_p|_K\boldsymbol{n}_K + \boldsymbol{\sigma}_p|_{K'}\boldsymbol{n}_{K'} = \boldsymbol{0},$$

so the contribution of each interior face to $\langle \boldsymbol{\sigma}_p\boldsymbol{n},\widehat{\boldsymbol{v}}\rangle_{\partial\mathcal{T}_h}$ is zero. On boundary faces $F \subset \Gamma_s$, we have $\widehat{\boldsymbol{v}}|_F = \boldsymbol{0}$ by definition of $\mathcal{M}_h$ (which enforces homogeneous Dirichlet conditions on Γ_s), so the boundary integral vanishes. On boundary faces $F \subset \Gamma_a$, the exact solution satisfies $\boldsymbol{\sigma}_p|_{\Omega_a} = -p\,\mathrm{I}_d$ with $p|_{\Gamma_a} = 0$ (sound-soft boundary condition), hence $\boldsymbol{\sigma}_p\boldsymbol{n}|_F = -p|_F\boldsymbol{n}|_F = \boldsymbol{0}$. Therefore, $\langle \boldsymbol{\sigma}_p\boldsymbol{n},\widehat{\boldsymbol{v}}\rangle_{\partial\mathcal{T}_h} = 0$, and by (5.4):

$$B_h(\boldsymbol{\sigma}_p,(\boldsymbol{v},\widehat{\boldsymbol{v}})) = (\mathbf{div}\,\boldsymbol{\sigma}_p,\boldsymbol{v})_\Omega = B(\boldsymbol{\sigma}_p,\boldsymbol{v}).$$

The same argument with $\widehat{\boldsymbol{u}} = \boldsymbol{u}|_{\mathcal{F}_h}$ shows that $B_h(\boldsymbol{\tau}_q,(\boldsymbol{u},\widehat{\boldsymbol{u}})) = B(\boldsymbol{\tau}_q,\boldsymbol{u})$. Substituting into the continuous equations (3.6) completes the proof. □

5.2 Stability of the semi-discrete problem

We now establish a stability estimate for the semi-discrete HDG formulation in terms of consistency errors. Throughout, $\Pi_{\mathcal{T}}^k$, $\Pi_{\mathcal{T}}^{k+1}$, and $\Pi_{\mathcal{F}}^{k+1}$ denote the L^2-orthogonal projectors onto the polynomial spaces $\mathcal{P}_k(\mathcal{T}_h)$, $\mathcal{P}_{k+1}(\mathcal{T}_h)$, and $\mathcal{P}_{k+1}(\mathcal{F}_h)$, respectively; their definitions and approximation properties are collected in Appendix A. Define the projected errors

$$\boldsymbol{\pi}_h := \boldsymbol{\sigma}_{p,h} - \Pi_{\mathcal{T}}^k\boldsymbol{\sigma}_p, \quad \boldsymbol{e}_h := \boldsymbol{u}_h - \Pi_{\mathcal{T}}^{k+1}\boldsymbol{u}, \quad \widehat{\boldsymbol{e}}_h := \widehat{\boldsymbol{u}}_h - \Pi_{\mathcal{F}}^{k+1}(\boldsymbol{u}|_{\mathcal{F}_h}),$$

and the approximation errors

$$\boldsymbol{\chi} := \boldsymbol{\sigma}_p - \Pi_{\mathcal{T}}^k \boldsymbol{\sigma}_p, \quad \boldsymbol{q} := \boldsymbol{u} - \Pi_{\mathcal{T}}^{k+1} \boldsymbol{u}, \quad \widehat{\boldsymbol{q}} := \boldsymbol{u}|_{\mathcal{F}_h} - \Pi_{\mathcal{F}}^{k+1}(\boldsymbol{u}|_{\mathcal{F}_h}) \,.$$

LEMMA 5.1 (Stability of projected errors). Under the conditions of Proposition 5.2, there exists a constant $C > 0$ independent of h and k such that

$$\begin{aligned} \max_{[0,T]} \|\boldsymbol{\pi}_h(t)\|_{\mathcal{H}^\sigma}^2 + \max_{[0,T]} \|\boldsymbol{e}_h(t)\|_{\mathcal{H}^u}^2 + \int_0^T \|\tfrac{k+1}{h_{\mathcal{F}}^{1/2}} \boldsymbol{\delta}_h(\boldsymbol{e}_h, \widehat{\boldsymbol{e}}_h)\|_{0,\partial\mathcal{T}_h}^2 \,\mathrm{d}t \\ \leq C \int_0^T \Big(|(\boldsymbol{q}, \widehat{\boldsymbol{q}})|_{1,h}^2 + \|\tfrac{h_{\mathcal{F}}^{1/2}}{k+1} \boldsymbol{\chi}\boldsymbol{n}\|_{0,\partial\mathcal{T}_h}^2 \Big) \mathrm{d}t \,. \end{aligned} \tag{5.5}$$

Proof. The proof derives error equations by subtracting the discrete from the continuous formulations, exploits orthogonality of L^2-projections to eliminate time derivatives of approximation errors, then applies energy methods with Gronwall's lemma to control the projected errors in terms of approximation errors. Using the consistency property from Proposition 5.2, we subtract the discrete equations (4.3) from the continuous equations tested with discrete functions to obtain

$$\begin{aligned} &(\dot{\boldsymbol{\pi}}_h, \boldsymbol{\tau}_q)_{\mathcal{H}^\sigma} + (\dot{\boldsymbol{e}}_h, \boldsymbol{v})_{\mathcal{H}^u} + B_h(\boldsymbol{\pi}_h, (\boldsymbol{v}, \widehat{\boldsymbol{v}})) - B_h(\boldsymbol{\tau}_q, (\boldsymbol{e}_h, \widehat{\boldsymbol{e}}_h)) + \langle \tfrac{(k+1)^2}{h_{\mathcal{F}}} \boldsymbol{\delta}_h(\boldsymbol{e}_h, \widehat{\boldsymbol{e}}_h), \boldsymbol{\delta}_h(\boldsymbol{v}, \widehat{\boldsymbol{v}}) \rangle_{\partial\mathcal{T}_h} \\ &\quad = \langle \boldsymbol{\chi}\boldsymbol{n}, (\boldsymbol{v} - \widehat{\boldsymbol{v}}) \rangle_{\partial\mathcal{T}_h} + B_h(\boldsymbol{\tau}_q, (\boldsymbol{q}, \widehat{\boldsymbol{q}})) - \langle \tfrac{(k+1)^2}{h_{\mathcal{F}}} \boldsymbol{\delta}_h(\boldsymbol{q}, \widehat{\boldsymbol{q}}), \boldsymbol{\delta}_h(\boldsymbol{v}, \widehat{\boldsymbol{v}}) \rangle_{\partial\mathcal{T}_h} \end{aligned} \tag{5.6}$$

for all $\boldsymbol{\tau}_q \in \mathcal{H}_h^\sigma$ and $(\boldsymbol{v}, \widehat{\boldsymbol{v}}) \in \mathcal{H}_h^u \times \mathcal{M}_h$, where the right-hand side follows from orthogonality properties of the L^2-projections. Indeed, since the material parameters are piecewise constant on $\mathcal{T}_h$:

$$(\dot{\boldsymbol{\chi}}, \boldsymbol{\tau}_q)_{\mathcal{H}^\sigma} = (\dot{\boldsymbol{\sigma}}_p - \Pi_{\mathcal{T}}^k \dot{\boldsymbol{\sigma}}_p, \mathcal{C}^{-1} \boldsymbol{\tau}_q)_{\Omega_s} + (c(p - \Pi_{\mathcal{T}}^k p), q)_{\Omega_a} = 0 \quad \forall \boldsymbol{\tau}_q \in \mathcal{H}_h^\sigma,$$

where we used that $\mathcal{C}^{-1}(\mathbf{x}) \mathcal{P}_k(\mathcal{T}_h, \mathbb{R}^{d\times d}_{\mathrm{sym}}) \subset \mathcal{P}_k(\mathcal{T}_h, \mathbb{R}^{d\times d}_{\mathrm{sym}})$ and $c(\mathbf{x}) \mathcal{P}_k(\mathcal{T}_h) \subset \mathcal{P}_k(\mathcal{T}_h)$. Similarly, because $\rho(\mathbf{x}) \mathcal{P}_{k+1}(\mathcal{T}_h, \mathbb{R}^d) \subset \mathcal{P}_{k+1}(\mathcal{T}_h, \mathbb{R}^d)$,

$$(\dot{\boldsymbol{q}}, \boldsymbol{v})_{\mathcal{H}^u} = (\dot{\boldsymbol{u}} - \Pi_{\mathcal{T}}^{k+1} \dot{\boldsymbol{u}}, \rho \boldsymbol{v})_{\Omega} = 0 \quad \forall \boldsymbol{v} \in \mathcal{P}_{k+1}(\mathcal{T}_h, \mathbb{R}^d).$$

Finally, as $\boldsymbol{\varepsilon}(\mathcal{P}_{k+1}(\mathcal{T}_h, \mathbb{R}^d)) \subset \mathcal{P}_k(\mathcal{T}_h, \mathbb{R}^{d\times d}_{\mathrm{sym}})$,

$$B_h(\boldsymbol{\chi}, (\boldsymbol{v}, \widehat{\boldsymbol{v}})) = -(\boldsymbol{\sigma}_p - \Pi_{\mathcal{T}}^k \boldsymbol{\sigma}_p, \boldsymbol{\varepsilon}(\boldsymbol{v}))_{\mathcal{T}_h} + \langle \boldsymbol{\chi}\boldsymbol{n}, (\boldsymbol{v} - \widehat{\boldsymbol{v}}) \rangle_{\partial\mathcal{T}_h} = \langle \boldsymbol{\chi}\boldsymbol{n}, (\boldsymbol{v} - \widehat{\boldsymbol{v}}) \rangle_{\partial\mathcal{T}_h} \quad \forall (\boldsymbol{v}, \widehat{\boldsymbol{v}}) \in \mathcal{H}_h^u \times \mathcal{M}_h.$$

Set $E(t) := \|\boldsymbol{\pi}_h(t)\|_{\mathcal{H}^\sigma}^2 + \|\boldsymbol{e}_h(t)\|_{\mathcal{H}^u}^2$. Taking $\boldsymbol{\tau}_q = \boldsymbol{\pi}_h$ and $(\boldsymbol{v}, \widehat{\boldsymbol{v}}) = (\boldsymbol{e}_h, \widehat{\boldsymbol{e}}_h)$ in (5.6), the two B_h terms on the left-hand side cancel. Since $\boldsymbol{\chi}\boldsymbol{n} = -(p - \Pi_{\mathcal{T}}^k p)\boldsymbol{n}$ is normal on acoustic-side interface faces, $\langle \boldsymbol{\chi}\boldsymbol{n}, \boldsymbol{e}_h - \widehat{\boldsymbol{e}}_h \rangle = \langle \boldsymbol{\chi}\boldsymbol{n}, \boldsymbol{\delta}_h(\boldsymbol{e}_h, \widehat{\boldsymbol{e}}_h) \rangle$ there. Applying the Cauchy–Schwarz inequality and Lemma 4.1 gives

$$\begin{aligned} \tfrac{1}{2} \dot{E}(t) + \|\tfrac{k+1}{h_{\mathcal{F}}^{1/2}} \boldsymbol{\delta}_h(\boldsymbol{e}_h, \widehat{\boldsymbol{e}}_h)\|_{0,\partial\mathcal{T}_h}^2 \;\leq\; & \|\tfrac{h_{\mathcal{F}}^{1/2}}{k+1} \boldsymbol{\chi}\boldsymbol{n}\|_{0,\partial\mathcal{T}_h} \|\tfrac{k+1}{h_{\mathcal{F}}^{1/2}} \boldsymbol{\delta}_h(\boldsymbol{e}_h, \widehat{\boldsymbol{e}}_h)\|_{0,\partial\mathcal{T}_h} \\ & + C \|\boldsymbol{\pi}_h\|_{\mathcal{H}^\sigma} |(\boldsymbol{q}, \widehat{\boldsymbol{q}})|_{1,h} + \|\tfrac{k+1}{h_{\mathcal{F}}^{1/2}} \boldsymbol{\delta}_h(\boldsymbol{q}, \widehat{\boldsymbol{q}})\|_{0,\partial\mathcal{T}_h} \|\tfrac{k+1}{h_{\mathcal{F}}^{1/2}} \boldsymbol{\delta}_h(\boldsymbol{e}_h, \widehat{\boldsymbol{e}}_h)\|_{0,\partial\mathcal{T}_h} \,. \end{aligned}$$

Assuming $\boldsymbol{\sigma}_{p,h}(0) = \Pi_{\mathcal{T}}^k \boldsymbol{\sigma}_p^0$ and $\boldsymbol{u}_h(0) = \Pi_{\mathcal{T}}^{k+1} \boldsymbol{u}^0$, so that $E(0) = 0$, Young's inequality $ab \leq \varepsilon a^2 + \frac{1}{4\varepsilon} b^2$ applied to each product on the right-hand side yields the differential inequality

$$\dot{E}(t) + \|\tfrac{k+1}{h_{\mathcal{F}}^{1/2}} \boldsymbol{\delta}_h(\boldsymbol{e}_h, \widehat{\boldsymbol{e}}_h)\|_{0,\partial\mathcal{T}_h}^2 \leq C E(t) + C \Big(\|\tfrac{h_{\mathcal{F}}^{1/2}}{k+1} \boldsymbol{\chi}\boldsymbol{n}\|_{0,\partial\mathcal{T}_h}^2 + |(\boldsymbol{q}, \widehat{\boldsymbol{q}})|_{1,h}^2 \Big).$$

Dropping the non-negative stabilization term from the left-hand side and applying Gronwall's lemma

with $E(0) = 0$ gives

$$E(t) \le Ce^{CT} \int_0^T \left(\| \tfrac{h_{\mathcal{F}}^{1/2}}{k+1} \boldsymbol{\chi} \boldsymbol{n} \|_{0,\partial\mathcal{T}_h}^2 + |(\boldsymbol{q}, \widehat{\boldsymbol{q}})|_{1,h}^2 \right) \mathrm{d}t \quad \forall t \in [0,T].$$

Integrating the differential inequality over $(0,T)$, using $E(0) = 0$, and substituting this bound for E on the right-hand side yields

$$\int_0^T \| \tfrac{k+1}{h_{\mathcal{F}}^{1/2}} \boldsymbol{\delta}_h(\boldsymbol{e}_h, \widehat{\boldsymbol{e}}_h) \|_{0,\partial\mathcal{T}_h}^2 \, \mathrm{d}t \le C \int_0^T \left(\| \tfrac{h_{\mathcal{F}}^{1/2}}{k+1} \boldsymbol{\chi} \boldsymbol{n} \|_{0,\partial\mathcal{T}_h}^2 + |(\boldsymbol{q}, \widehat{\boldsymbol{q}})|_{1,h}^2 \right) \mathrm{d}t,$$

which completes the proof. □

5.3 Convergence theorem

The following result establishes *hp*-convergence rates for the semi-discrete HDG formulation.

THEOREM 5.1 (hp-Convergence). Let

$$\boldsymbol{\sigma}_p \in \mathcal{C}^1([0,T]; \mathcal{H}^\sigma) \cap \mathcal{C}^0([0,T]; \mathcal{X}^\sigma) \quad \text{and} \quad \boldsymbol{u} \in \mathcal{C}^1([0,T]; \mathcal{H}^u) \cap \mathcal{C}^0([0,T]; \mathcal{X}^u)$$

be the solutions of (3.6). Assume further that

$$\boldsymbol{\sigma}_p \in \mathcal{C}^0([0,T]; H^{1+r}(\mathcal{T}_h, \mathbb{R}^{d\times d}_{\mathrm{sym}}) \cap \mathcal{H}^\sigma) \quad \text{and} \quad \boldsymbol{u} \in \mathcal{C}^0([0,T]; H^{2+r}(\Omega, \mathbb{R}^d)),$$

with $r \ge 0$. Then, there exists a constant $C > 0$ independent of h and k such that

$$\begin{aligned} &\max_{t\in[0,T]} \|(\boldsymbol{\sigma}_p - \boldsymbol{\sigma}_{p,h})(t)\|_{\mathcal{H}^\sigma} + \max_{t\in[0,T]} \|(\boldsymbol{u} - \boldsymbol{u}_h)(t)\|_{\mathcal{H}^u} + \left(\int_0^T \| \tfrac{k+1}{h_{\mathcal{F}}^{1/2}} \boldsymbol{\delta}_h(\boldsymbol{u}, \widehat{\boldsymbol{u}}_h) \|_{0,\partial\mathcal{T}_h}^2 \, \mathrm{d}t \right)^{1/2} \\ &\quad \le C \tfrac{h^{\min\{r,k\}+1}}{(k+1)^{r+1/2}} \Big(\max_{t\in[0,T]} \|\boldsymbol{\sigma}_p(t)\|_{1+r,\Omega_s}^2 + \max_{t\in[0,T]} \|p(t)\|_{1+r,\Omega_a}^2 + \max_{t\in[0,T]} \|\boldsymbol{u}(t)\|_{2+r,\Omega}^2 \Big)^{1/2} \quad \forall k \ge 0. \end{aligned}$$

Proof. The triangle inequality and the stability estimate (5.5) give

$$\begin{aligned} &\max_{t\in[0,T]} \|(\boldsymbol{\sigma}_p - \boldsymbol{\sigma}_{p,h})(t)\|_{\mathcal{H}^\sigma}^2 + \max_{t\in[0,T]} \|(\boldsymbol{u} - \boldsymbol{u}_h)(t)\|_{\mathcal{H}^u}^2 + \int_0^T \| \tfrac{k+1}{h_{\mathcal{F}}^{1/2}} \boldsymbol{\delta}_h(\boldsymbol{e}_h, \widehat{\boldsymbol{e}}_h) \|_{0,\partial\mathcal{T}_h}^2 \, \mathrm{d}t \\ &\quad \le \max_{t\in[0,T]} \|\boldsymbol{\chi}(t)\|_{\mathcal{H}^\sigma}^2 + \max_{t\in[0,T]} \|\boldsymbol{q}(t)\|_{\mathcal{H}^u}^2 + C \int_0^T \left(|(\boldsymbol{q}, \widehat{\boldsymbol{q}})|_{1,h}^2 + \| \tfrac{h_{\mathcal{F}}^{1/2}}{k+1} \boldsymbol{\chi} \boldsymbol{n} \|_{0,\partial\mathcal{T}_h}^2 \right) \mathrm{d}t. \end{aligned}$$

It remains to bound each approximation error on the right-hand side. Applying (A.2) componentwise to the stress-pressure field gives

$$\begin{aligned} \|\boldsymbol{\chi}\|_{\mathcal{H}^\sigma} &\le C \tfrac{h^{\min\{r,k\}+1}}{(k+1)^{r+1}} \Big(\|\boldsymbol{\sigma}\|_{1+r,\Omega_s}^2 + \|p\|_{1+r,\Omega_a}^2 \Big)^{1/2}, \\ \| \tfrac{h_{\mathcal{F}}^{1/2}}{k+1} \boldsymbol{\chi} \boldsymbol{n} \|_{0,\partial\mathcal{T}_h} &\le C \tfrac{h^{\min\{r,k\}+1}}{(k+1)^{r+1}} \Big(\|\boldsymbol{\sigma}\|_{1+r,\Omega_s}^2 + \|p\|_{1+r,\Omega_a}^2 \Big)^{1/2}. \end{aligned}$$

For the velocity field, Lemma A.3 gives

$$|(\boldsymbol{q}, \widehat{\boldsymbol{q}})|_{1,h} \le C \tfrac{h^{\min\{r,k\}+1}}{(k+1)^{r+1/2}} \|\boldsymbol{u}\|_{2+r,\Omega}.$$

Substituting these three bounds into the first estimate completes the proof. □

REMARK 5.1. The convergence analysis in Theorem 5.1 exhibits two types of suboptimality:

- The theoretical bound is suboptimal by a factor $(k+1)^{-1/2}$. This slight deterioration is common to hp-DG methods (cf. [8]).
- The numerical experiments of Subsections 6.1 and 6.1 suggest that $\boldsymbol{u}$ converges at the optimal rate $O(h^{k+2})$ in the L^2-norm, one order beyond what Theorem 5.1 guarantees. This improved L^2 estimate is expected from an Aubin–Nitsche duality argument, but carrying it out for the present coupled hyperbolic system remains an open problem.

6 Numerical results

The numerical results presented in this section have been implemented using the finite element library `Netgen/NGSolve` [16].

6.1 Validation of the convergence rates

We confirm the h- and k-convergence rates predicted by Theorem 5.1 in two regimes: a well-conditioned non-stiff case with moderate parameters, and a physically stiff case modelling soft tissue in water. We proceed by successive levels of refinement on an unstructured mesh. The computational domain is $\Omega = (0,1)\times(0,1)\cup(0,1)\times(-1,0)$, with the fluid region $\Omega_a = (0,1)\times(0,1)$ and the solid region $\Omega_s = (0,1)\times(-1,0)$ sharing the interface $\Sigma = (0,1)\times\{0\}$. We prescribe Dirichlet boundary conditions on $\Gamma_s = \partial\Omega_s \setminus \Sigma$ for the velocity, and sound-soft conditions on $\Gamma_a = \partial\Omega_a \setminus \Sigma$ for the pressure. The computed solutions are compared to a manufactured exact solution of problem (2.1)–(2.5) given by

$$\begin{aligned} p(x,y,t) &:= \sin(\pi t)\sin(\pi x)\sin(\pi y), \\ \boldsymbol{u}(x,y,t) &:= \sin(\pi t)\begin{pmatrix}\sin(\pi x)\sin(\pi(y+1)) \\ (y+1)\cos(\pi(x+\frac{1}{2}))\end{pmatrix}, \end{aligned} \tag{6.1}$$

in $\Omega\times(0,T]$. Source terms for (2.1) and (2.3) are computed so that (6.1) satisfies the governing equations with the chosen material parameters. We evaluate the following energy-norm error measures at the final time T:

$$\begin{aligned} \mathsf{e}_{hk}(\boldsymbol{\sigma},p) &:= \|(\boldsymbol{\sigma}_p - \boldsymbol{\sigma}_{p,h}^L)(T)\|_{\mathcal{H}^\sigma}, \\ \mathsf{e}_{hk}(\boldsymbol{u}) &:= \|(\boldsymbol{u} - \boldsymbol{u}_h^L)(T)\|_{\mathcal{H}^u}, \end{aligned} \tag{6.2}$$

where the superscript L denotes the number of time steps.

h-convergence: non-stiff regime

We consider an isotropic elastic solid with Lamé parameters $\mu = 50$, $\lambda = 500$, acoustic compressibility $c = 1$, and unit densities $\rho_s = \rho_a = 1$. The final time is $T = 0.5$; the entire solid boundary carries Neumann conditions ($\Gamma_s^N = \Gamma_s$) and the entire acoustic boundary carries Dirichlet conditions ($\Gamma_a^D = \Gamma_a$). Since the manufactured global stress tensor $\boldsymbol{\sigma}_p$ is discontinuous across Σ, its jump in normal components enters the right-hand side as

$$\int_\Sigma (\boldsymbol{\sigma}\boldsymbol{n}_s - p\,\boldsymbol{n}_a)\cdot\widehat{\boldsymbol{v}}\,\mathrm{d}s.$$

We discretize in time with the Crank-Nicolson scheme. Its second-order accuracy motivates the choice $\Delta t = O(h^{(k+2)/2})$, which ensures $(\Delta t)^2 \sim h^{k+2}$ and keeps the temporal error asymptotically dominated by the spatial error. In Table 6.1, we present the errors as functions of the mesh size h for polynomial degrees $k = 0, 1, 2$. In Figure 6.1, the errors (6.2) are displayed in log-log plots, with the expected rates of convergence represented by dashed lines. The results show that $\mathsf{e}_{hk}(\boldsymbol{\sigma}, p)$ and $\mathsf{e}_{hk}(\boldsymbol{u})$ achieve the optimal convergence rates of $O(h^{k+1})$ and $O(h^{k+2})$, respectively, in full agreement with Theorem 5.1.

k	h	L	$\mathsf{e}_{hk}(\boldsymbol{\sigma}, p)$	roc	$\mathsf{e}_{hk}(\boldsymbol{u})$	roc
0	1/32	16	$9.54 \cdot 10^{-1}$	*	$1.60 \cdot 10^{-1}$	*
	1/64	32	$4.65 \cdot 10^{-1}$	1.04	$3.72 \cdot 10^{-2}$	2.10
	1/128	64	$2.29 \cdot 10^{-1}$	1.02	$9.04 \cdot 10^{-3}$	2.04
	1/256	128	$1.14 \cdot 10^{-1}$	1.01	$2.22 \cdot 10^{-3}$	2.03
1	1/16	32	$5.81 \cdot 10^{-2}$	*	$5.26 \cdot 10^{-3}$	*
	1/32	91	$1.35 \cdot 10^{-2}$	2.11	$6.27 \cdot 10^{-4}$	3.07
	1/64	256	$3.12 \cdot 10^{-3}$	2.11	$7.78 \cdot 10^{-5}$	3.01
	1/128	724	$7.85 \cdot 10^{-4}$	1.99	$9.94 \cdot 10^{-6}$	2.97
2	1/8	32	$1.03 \cdot 10^{-2}$	*	$1.01 \cdot 10^{-3}$	*
	1/16	128	$1.16 \cdot 10^{-3}$	3.14	$6.11 \cdot 10^{-5}$	4.05
	1/32	512	$1.29 \cdot 10^{-4}$	3.17	$3.36 \cdot 10^{-6}$	4.18
	1/64	2048	$1.49 \cdot 10^{-5}$	3.12	$2.04 \cdot 10^{-7}$	4.04

Table 6.1: Non-stiff regime: error progression and convergence rates for uniform h-refinements with polynomial degrees $k = 0, 1, 2$. The time step $\Delta t = O(h^{(k+2)/2})$ ensures that the Crank-Nicolson temporal error remains subordinate. The number of time steps L corresponds to a uniform subdivision of $[0, T]$ with $T = 0.5$. Errors are measured at the final time using the manufactured solution (6.1).

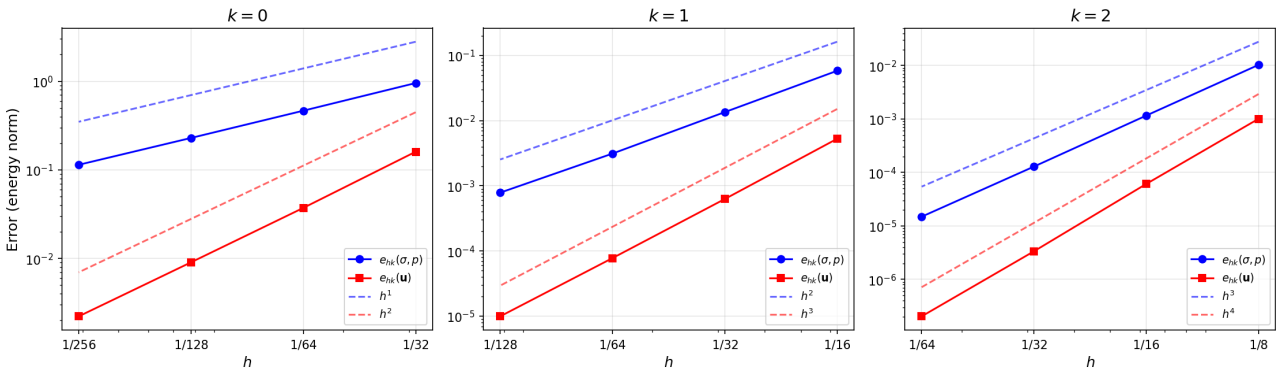

Figure 6.1: Non-stiff regime: the errors (6.2) are plotted against the mesh size h for polynomial degrees $k = 0, 1, 2$, with dashed lines indicating the reference slopes h^{k+1} and h^{k+2}.

h-convergence: stiff regime

To demonstrate robustness in a physically relevant stiff setting, we consider a medical ultrasound scenario: a nearly incompressible solid coupled to water. The solid is characterized by Young's modulus $E = 3 \times 10^4\,\mathrm{Pa}$ and Poisson's ratio $\nu = 0.49999$, giving Lamé coefficients $\lambda = \frac{E\nu}{(1+\nu)(1-2\nu)} \approx 5 \times 10^8\,\mathrm{Pa}$ and $\mu = \frac{E}{2(1+\nu)} \approx 10^4\,\mathrm{Pa}$, hence $\lambda/\mu \approx 50{,}000$. The acoustic compressibility is $c = 4.44 \times 10^{-10}\,\mathrm{Pa}^{-1}$ (water, $c_{\mathrm{sound}} \approx 1500\,\mathrm{m/s}$), and the densities are $\rho_s = 1050\,\mathrm{kg/m}^3$ (muscle tissue) and $\rho_a = 1000\,\mathrm{kg/m}^3$. The final time is $T = 0.5$; both boundaries carry homogeneous Dirichlet conditions ($\Gamma_s^D = \Gamma_s$, $\Gamma_a^D = \Gamma_a$). We employ the 5-stage, 4th-order L-stable SDIRK method of Hairer–Wanner for this study, because the Crank–Nicolson time step scaling $\Delta t = O(h^{(k+2)/2})$ makes runs with $k \geq 3$ on the meshes required for convergence computationally prohibitive. The L-stability of SDIRK4

avoids stiffness-induced instability at the intermediate Runge–Kutta stages. Due to well-known order reduction for implicit Runge–Kutta methods [7], caused here by the time-dependent interface forcing $\int_\Sigma (\boldsymbol{\sigma}\boldsymbol{n}_s - p\,\boldsymbol{n}_a)\cdot\widehat{\boldsymbol{v}}\,\mathrm{d}s$, the effective temporal order reduces from 4 to 3 (see Figure 6.5), and we set $\Delta t = O(h^{(k+2)/3})$.

Remark 6.1 (Comparison with Crank–Nicolson). Crank–Nicolson (A-stable, order 2) is the preferred integrator for the well-conditioned regime: it requires only one solve per step and the simpler time-step scaling $\Delta t = h^{(k+2)/2}$. SDIRK4 is used in the stiff regime (nearly incompressible solid or low-compressibility fluid), where its L-stability is essential to damp high-frequency spurious modes that CN leaves undamped. Despite the five-stage overhead, the larger admissible step $\Delta t = h^{(k+2)/3}$ and effective order 3 make it competitive.

In Table 6.2, we present the errors for polynomial degrees $k = 3, 4, 5$, and the corresponding log-log plots are displayed in Figure 6.2. The results confirm that the expected optimal spatial convergence rates—$O(h^{k+1})$ for $\mathsf{e}_{hk}(\boldsymbol{\sigma}, p)$ and $O(h^{k+2})$ for $\mathsf{e}_{hk}(\boldsymbol{u})$—are achieved despite the extreme stiffness ratio $\lambda/\mu \approx 50{,}000$. This robustness indicates the absence of volumetric locking, consistent with the first-order stress-velocity formulation using L^2 stress components.

k	h	L	$\mathsf{e}_{hk}(\boldsymbol{\sigma}, p)$	roc	$\mathsf{e}_{hk}(\boldsymbol{u})$	roc
3	1/8	16	$2.03 \cdot 10^{1}$	*	$3.94 \cdot 10^{2}$	*
	1/16	51	$1.19 \cdot 10^{0}$	4.09	$1.28 \cdot 10^{1}$	4.95
	1/32	161	$6.84 \cdot 10^{-2}$	4.12	$3.64 \cdot 10^{-1}$	5.13
	1/64	512	$3.36 \cdot 10^{-3}$	4.35	$1.05 \cdot 10^{-2}$	5.12
4	1/8	32	$4.18 \cdot 10^{-1}$	*	$3.62 \cdot 10^{0}$	*
	1/16	128	$1.16 \cdot 10^{-2}$	5.17	$5.18 \cdot 10^{-2}$	6.13
	1/32	512	$3.24 \cdot 10^{-4}$	5.16	$6.05 \cdot 10^{-4}$	6.42
	1/64	2048	$7.56 \cdot 10^{-6}$	5.42	$8.16 \cdot 10^{-6}$	6.21
5	1/4	13	$1.52 \cdot 10^{0}$	*	$2.52 \cdot 10^{1}$	*
	1/8	64	$1.26 \cdot 10^{-2}$	6.91	$1.52 \cdot 10^{-1}$	7.37
	1/16	323	$1.78 \cdot 10^{-4}$	6.15	$1.11 \cdot 10^{-3}$	7.11
	1/32	1625	$2.61 \cdot 10^{-6}$	6.09	$7.36 \cdot 10^{-6}$	7.23

Table 6.2: Stiff regime (soft tissue in water): error progression and convergence rates for uniform h-refinements with polynomial degrees $k = 3, 4, 5$. The SDIRK4 time step $\Delta t = O(h^{(k+2)/3})$ accounts for order reduction to effective temporal order 3. The number of time steps L corresponds to $T = 0.5$. Errors are measured at the final time using the manufactured solution (6.1).

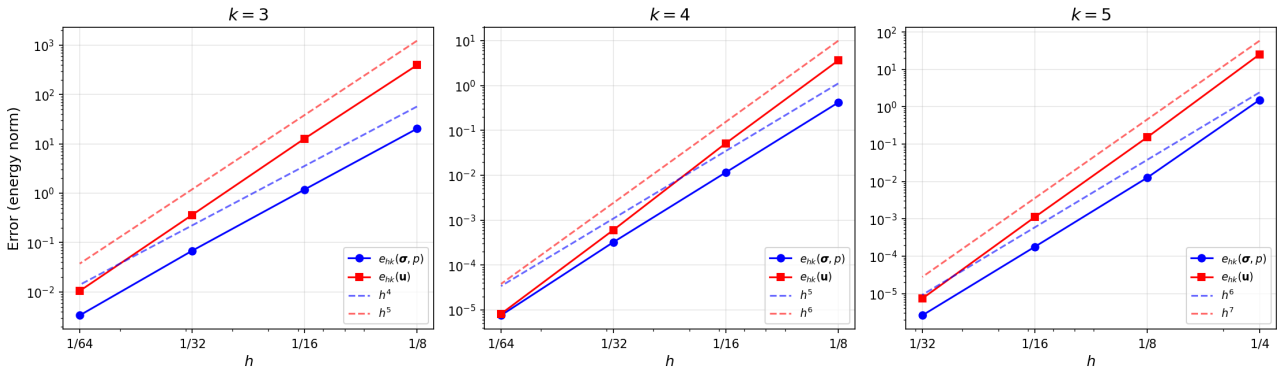

Figure 6.2: Stiff regime: the errors (6.2) are plotted against h for polynomial degrees $k = 3, 4, 5$, with dashed lines indicating the reference slopes h^{k+1} and h^{k+2}.

p-convergence and temporal convergence

Having established the scheme's behavior with respect to the mesh size h, we now turn to testing its performance with respect to the polynomial degree k and the time step Δt. We fix the mesh size at $h = 1/10$ and the time step at $\Delta t = 10^{-4}$ (small enough for temporal errors to be negligible), and let the polynomial degree k vary from 0 to 6. The SDIRK4 method is used for time integration, with material parameters $\mu = 50$, $\lambda = 500$, $c = 1$, $\rho_s = \rho_a = 1$, and final time $T = 0.3$. In Figure 6.3, we present the errors $\mathsf{e}_{hk}(\boldsymbol{\sigma}, p)$ and $\mathsf{e}_{hk}(\boldsymbol{u})$ plotted against the polynomial degree k on a semi-logarithmic scale. As expected from Theorem 5.1, exponential convergence is observed, with both error measures decreasing at a rate consistent with $\exp(-\alpha k)$, $\alpha \approx 3.6$. Next, we isolate the temporal discretization error by fixing the spatial mesh at $h = 1/32$ and the polynomial degree at $k = 3$, with the same non-stiff parameters. We uniformly subdivide $[0, T]$ with $T = 0.5$ and vary the time step $\Delta t = 2^{-(l+1)}$ for $l = 0, 1, \ldots, 7$. Figure 6.4 shows the temporal convergence for the Crank–Nicolson scheme: the expected rate of $O(\Delta t^2)$ is achieved. Figure 6.5 shows the corresponding results for SDIRK4: both error measures converge at rate $O(\Delta t^3)$, confirming the order reduction from the classical order 4 to an effective order 3 due to the time-dependent boundary conditions, as discussed in Section B.

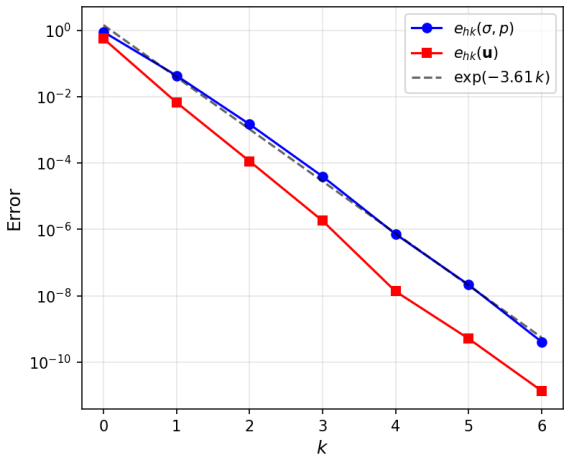

Figure 6.3: Computed errors versus the polynomial degree k with $h = 1/10$ and $\Delta t = 10^{-4}$. The errors are measured at $T = 0.3$, using the non-stiff parameters.

6.2 Ricker wavelet benchmark: qualitative propagation and semi-analytical validation

We validate the qualitative behaviour of our HDG method on a wave propagation benchmark introduced by Mottier et al. [14] for the Hybrid High-Order (HHO) method. Following the academic setting of [14, Sec. 6.4.1], the domain $\Omega = \Omega_a \cup \Omega_s$ consists of a fluid slab overlying a solid slab,

$$\Omega_a = \left(-\tfrac{1}{2}, \tfrac{1}{2}\right) \times \left(0, \tfrac{1}{2}\right), \qquad \Omega_s = \left(-\tfrac{1}{2}, \tfrac{1}{2}\right) \times \left(-\tfrac{1}{2}, 0\right), \tag{6.3}$$

sharing the interface $\Sigma = (-\frac{1}{2}, \frac{1}{2}) \times \{0\}$. The material parameters are set to

$$\rho_a = \rho_s = 1, \qquad \mu = \lambda = 1, \qquad c = 1, \tag{6.4}$$

yielding compressional speeds $c_P^F = (c\rho_a)^{-1/2} = 1$ in the fluid and $c_P^S = [(\lambda + 2\mu)/\rho_s]^{1/2} = \sqrt{3}$ in the solid, together with shear speed $c_S^S = (\mu/\rho_s)^{1/2} = 1$. Homogeneous Dirichlet conditions $p = 0$ on Γ_a and $\boldsymbol{u}_s = \mathbf{0}$ on Γ_s are imposed, with all volume sources set to zero. The initial stress, solid velocity,

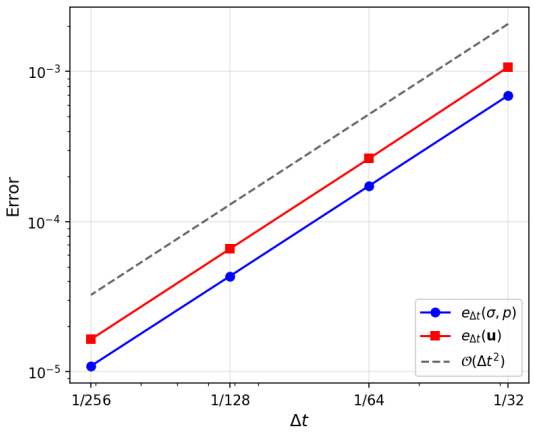

Figure 6.4: Temporal convergence for Crank–Nicolson with $h = 1/32$ and $k = 3$. The errors are measured at $T = 0.5$, with the non-stiff parameters. The dashed line indicates the reference slope $O(\Delta t^2)$.

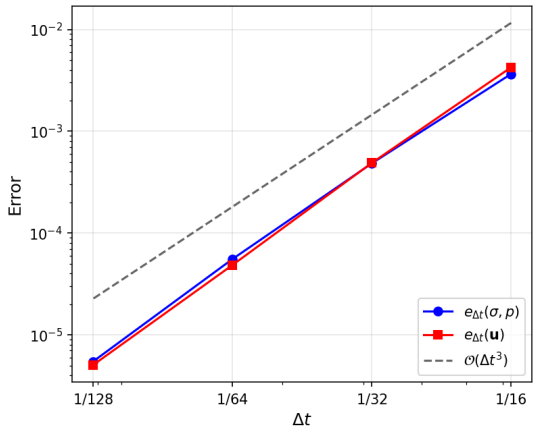

Figure 6.5: Temporal convergence for SDIRK4 with $h = 1/32$ and $k = 3$. The errors are measured at $T = 0.5$, with the non-stiff parameters. The dashed line indicates the reference slope $O(\Delta t^3)$, confirming the effective order reduction from 4 to 3.

and fluid pressure vanish; the sole initial datum is a velocity Ricker wavelet confined to Ω_a,

$$\boldsymbol{u}_a^0(x, y) = \theta \exp\Big(-\frac{\pi^2 r^2}{\Lambda^2}\Big) \begin{pmatrix} x - x_c \\ y - y_c \end{pmatrix}, \qquad r^2 = (x - x_c)^2 + (y - y_c)^2, \tag{6.5}$$

with central frequency $f_c = 10$, characteristic wavelength $\Lambda = c_P^F / f_c = 0.1$, and pulse center $(x_c, y_c) = (0, 0.125)$. The HDG method of Section 4 is used with Crank–Nicolson time integration throughout. Two sets of numerical experiments are reported, corresponding to Figures 9 and 10 of [14], respectively. For the spatial snapshots of Figure 6.6, we use polynomial degree $k = 4$, mesh size $h = 1/40$, time step $\Delta t = 5 \times 10^{-4}$, and $\theta = 10$ as in [14]. The acoustic pressure in Ω_a and the elastic velocity magnitude $\|\boldsymbol{u}_s\|$ in Ω_s are displayed at $t \in \{0.25, 0.27, 0.32\}$, matching the output times of Figure 9 in [14]. At $t = 0.25$, the Ricker pulse centred at $(0, 0.125) \in \Omega_a$ has propagated outward and reached Σ. By $t = 0.27$, a transmitted compressional P-wave (speed $c_P^S = \sqrt{3}$) is visible in the solid, alongside a slower shear S-wave (speed $c_S^S = 1$), while the reflected acoustic wave continues to spread through Ω_a. At $t = 0.32$, the P-wave has clearly separated from the S-wave and energy has been redistributed between the two subdomains, reflecting the material contrast at Σ. These features are in full qualitative agreement with Figure 9 of [14], obtained with the HHO method and SDIRK(3,4) time integration. For the sensor time histories of Figure 6.7, we use $k \in \{3, 4, 5\}$, $h = 1/16$, $\Delta t = 10^{-3}$, $T = 0.25$, and $\theta = 3.5 \times 10^4$ (chosen to match the amplitude of the semi-analytical reference; the signal shape is independent of θ by linearity). To validate our results, we compare them against the semi-analytical solution obtained using the open source software `Gar6more2D`[1]. The acoustic pressure is sampled at the fluid sensor $S^F = (-0.15, 0.1)$ and the two solid velocity components at the elastic sensor $S^S = (-0.15, -0.1)$. We note that our fluid momentum equation (2.3a) uses the sign convention $\rho_a \dot{\boldsymbol{u}}_a + \nabla p = \mathbf{0}$, whereas [14] and `Gar6more2D` adopt the convention $\rho_a \dot{\boldsymbol{u}}_a - \nabla p = \mathbf{0}$. Accordingly, we plot $-p$ at S^F to align with the semi-analytical reference. The three curves for $k = 3, 4, 5$ are essentially indistinguishable over $[0, 0.25]$, confirming that the HDG solution is well-resolved on $h = 1/16$ for $k \geq 4$. The main acoustic pulse arrives at S^F near $t \approx 0.15$; the elastic response recorded at S^S shows the compressional P-wave arriving before the slower shear component. The $k = 4$ and $k = 5$ solutions

[1] Available at `https://gitlab.inria.fr/jdiaz/gar6more2d`

are essentially indistinguishable from the `Gar6more2D` reference, confirming that the spatial error is negligible for $k \geq 4$ at this resolution.

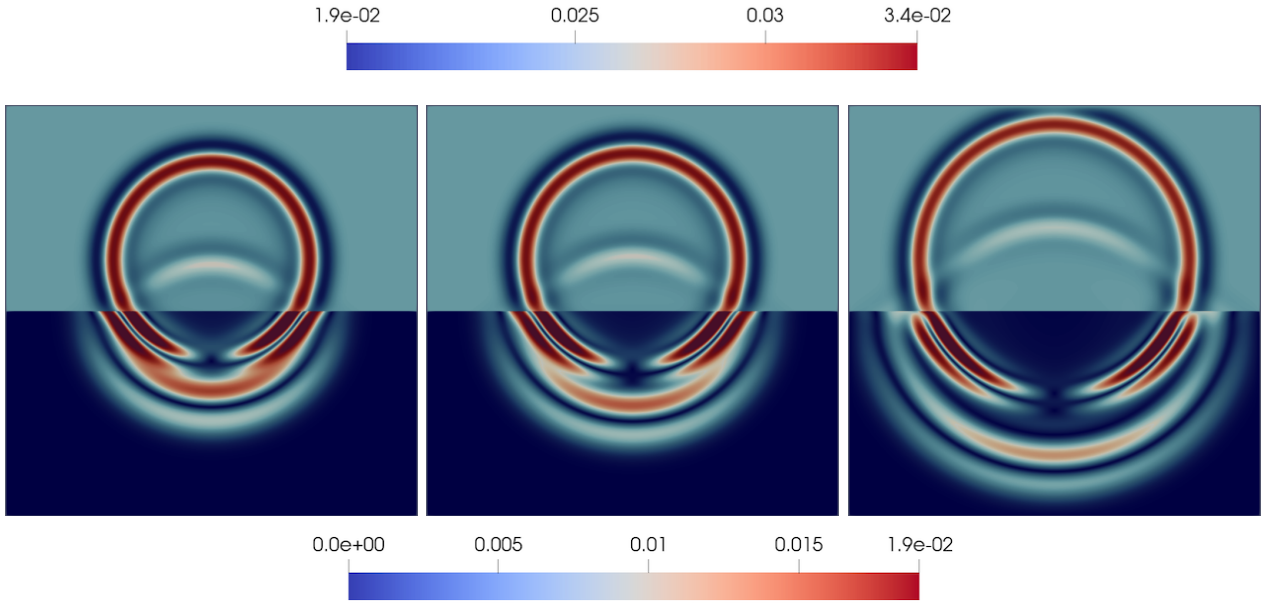

Figure 6.6: Academic Ricker wavelet test case [14]: spatial distribution of the acoustic pressure p in Ω_a (upper half) and the elastic velocity magnitude $\|\boldsymbol{u}_s\|$ in Ω_s (lower half), at times $t = 0.25$ (left), $t = 0.27$ (centre), and $t = 0.32$ (right). Computed with the HDG scheme using $k = 4$, $h = 1/40$, $\Delta t = 5 \times 10^{-4}$, $\theta = 10$, and Crank–Nicolson time integration.

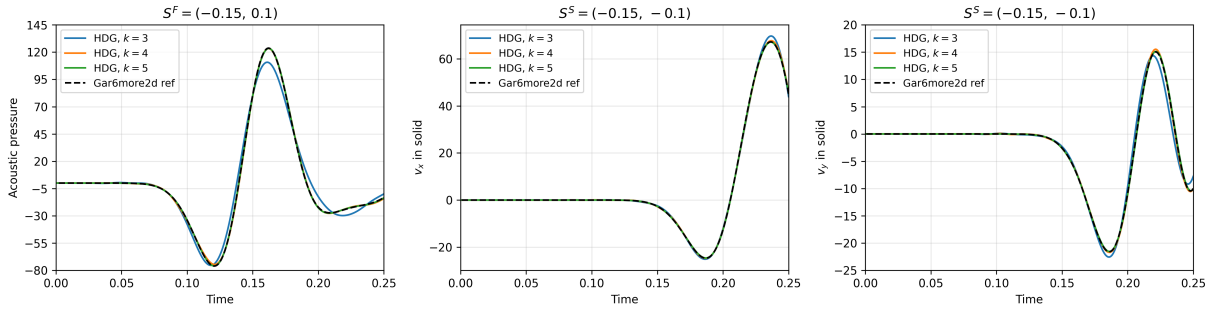

Figure 6.7: Academic Ricker wavelet test case [14]: time histories of $-p$ at the fluid sensor $S^F = (-0.15, 0.1)$ (left panel) and of the solid velocity components v_x (centre) and v_y (right) at the elastic sensor $S^S = (-0.15, -0.1)$, for polynomial degrees $k = 3, 4, 5$. Computed with the HDG scheme using $h = 1/16$, $\Delta t = 10^{-3}$, $T = 0.25$, $\theta = 3.5 \times 10^4$, and Crank–Nicolson time integration. The pressure is negated to match the sign convention of [14] ($\rho_a \dot{\boldsymbol{u}}_a - \nabla p = \boldsymbol{0}$), which differs from ours by a sign in p.

6.3 Ricker wavelet benchmark: ocean-crust interface and absorbing boundary conditions

As a further qualitative benchmark, we revisit the elastic–acoustic interface test of [18, Sec. 7.2]. The computational domain consists of two homogeneous half-spaces,

$$\Omega_a = (-4000, 4000) \times (0, 2500) \text{ m}, \qquad \Omega_s = (-4000, 4000) \times (-3500, 0) \text{ m}, \tag{6.6}$$

representing an acoustic ocean layer overlying an elastic crustal half-space, separated by a horizontal interface Σ at $y = 0$. The material parameters are

$$\rho_a = 1020\ \mathrm{kg\,m^{-3}}, \quad c_P^F = 1500\ \mathrm{m\,s^{-1}}, \quad \rho_s = 2500\ \mathrm{kg\,m^{-3}}, \quad c_P^S = 3600\ \mathrm{m\,s^{-1}}, \quad c_S^S = 2000\ \mathrm{m\,s^{-1}}. \tag{6.7}$$

These values yield Lamé parameters $\mu = \rho_s (c_S^S)^2 = 10^{10}$ Pa and $\lambda = \rho_s (c_P^S)^2 - 2\mu = 1.24 \times 10^{10}$ Pa, bulk modulus $\kappa = \rho_a (c_P^F)^2 = 2.295 \times 10^9$ Pa, and compressibility $c = \kappa^{-1}$. The source models a pure explosion (isotropic moment tensor) located at $(x_s,\, y_s) = (0,\, 650)$ m in the acoustic domain. Following [18], the source enters the acoustic mass conservation equation as a right-hand side $g(x, y, t) = A\, \mathcal{R}(t)\, \varphi(x, y)$, where

$$\mathcal{R}(t) = \left[1 - 2\pi^2 f_c^2 (t - t_0)^2\right] \mathrm{e}^{-\pi^2 f_c^2 (t - t_0)^2} \tag{6.8}$$

is the Ricker wavelet with central frequency $f_c = 5$ Hz and time delay $t_0 = 0.5$ s, and $A = 10^{11}$. The point source of [18] is regularised here as a normalised Gaussian of half-width $\sigma_{\mathrm{src}} = 60$ m ($\approx 1.5\, h$), so that the source is well resolved on the computational mesh. Whereas [18] confines the wavefield with ADE-PML layers at all exterior boundaries, we impose first-order absorbing boundary conditions. On the solid boundary Γ_s we apply the Lysmer–Kuhlemeyer condition [10],

$$\boldsymbol{\sigma}\, \boldsymbol{n} = Z_P\, (\boldsymbol{u} \cdot \boldsymbol{n})\, \boldsymbol{n} + Z_S\, [\boldsymbol{u} - (\boldsymbol{u} \cdot \boldsymbol{n})\, \boldsymbol{n}], \tag{6.9}$$

where $Z_P = \rho_s c_P^S$ and $Z_S = \rho_s c_S^S$ are the P- and S-wave impedances of the solid. On the fluid boundary Γ_a we apply the Sommerfeld condition $p = Z_F\, (\boldsymbol{u} \cdot \boldsymbol{n})$ with acoustic impedance $Z_F = \rho_a c_P^F$. These impedance conditions are exact for normally incident plane waves; at oblique incidence they introduce reflections that remain negligible over the displayed time window $t \in [0, 2]$ s, before off-angle reflections from the boundaries could corrupt the interior solution. The conditions (6.9) are incorporated at the discrete level as symmetric boundary bilinear forms added to the HDG system, in the same implicit Crank–Nicolson framework as the interior operator.

The HDG method of Section 4 is used with polynomial degree $k = 4$, element size $h = 40$ m, and time step $\Delta t = 5 \times 10^{-3}$ s, integrated up to $T = 2$ s with Crank–Nicolson. Snapshots of the velocity magnitude $\|\boldsymbol{u}\|$ over the full domain $\Omega = \Omega_a \cup \Omega_s$ at $t \in \{1.0,\, 1.5,\, 1.8\}$ s are shown in Figure 6.8. The simulation correctly reproduces all of the wave phenomena identified in Figure 10 of [18]. At $t = 1.0$ s the outward-expanding spherical pressure wave from the explosion is clearly visible in Ω_a, together with its partial reflection at Σ and the leading edge of the transmitted compressional P-wave in Ω_s. By $t = 1.5$ s, the transmitted P-wave (propagation speed $c_P^S = 3600$ m/s) has penetrated deep into the solid, while the slower converted P-to-S shear front (speed $c_S^S = 2000$ m/s) is distinctly separated and clearly visible as a lower-amplitude trailing wave. At $t = 1.8$ s the evanescent interface Scholte wave, whose phase speed lies just below c_S^S, has detached from the bulk S-wave and propagates as a guided mode along Σ. Also visible at $t = 1.8$ s are the head waves (von Schmidt waves) in Ω_s: straight wavefronts connecting the P- and S-fronts on each side, generated by the P-wave head wave running along Σ at speed c_P^S, which re-radiates S-waves into the solid at an oblique angle to the interface. These features—the direct and reflected acoustic pulse, the P-to-P and P-to-S transmitted fronts, the head waves in Ω_s, and the Scholte interface wave—are all present in our HDG solution with amplitudes and arrival times consistent with those reported in [18, Fig. 10], confirming that the HDG scheme correctly handles the wave transmission and mode conversion across the fluid–solid interface.

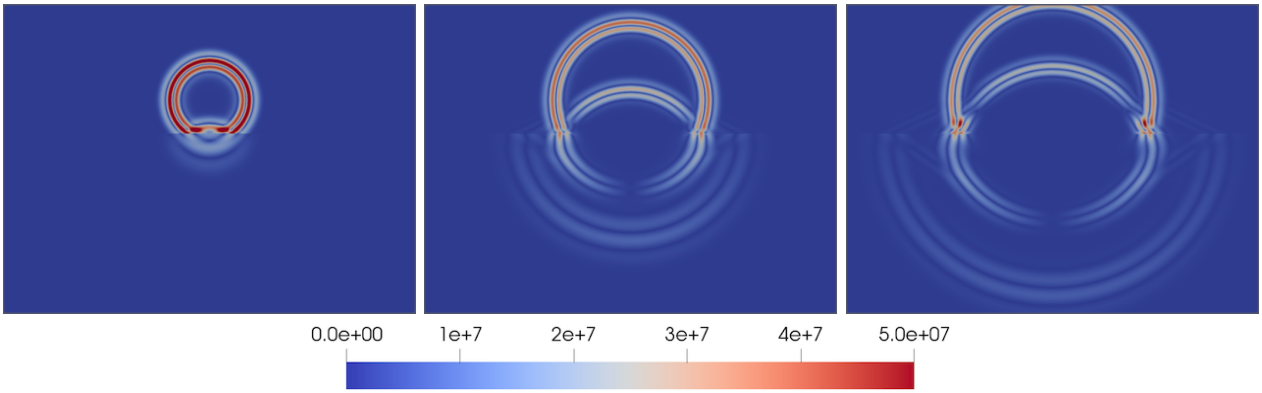

Figure 6.8: Elastic–acoustic interface benchmark [18, Sec. 7.2]: snapshots of the velocity magnitude $\|\boldsymbol{u}\|$ over the full domain $\Omega = \Omega_a \cup \Omega_s$, at $t = 1.0$ s (left), $t = 1.5$ s (centre), and $t = 1.8$ s (right). Computed with the HDG scheme using $k = 4$ (stress/pressure), $k{+}1 = 5$ (velocity), $h = 40$ m, $\Delta t = 5 \times 10^{-3}$ s, and Crank–Nicolson time integration. Exterior boundaries carry first-order absorbing conditions (Lysmer–Kuhlemeyer [10] on Γ_s, Sommerfeld on Γ_a). The expanding acoustic pulse, the transmitted P-wave and the converted P-to-S shear front in Ω_s, the head waves connecting the P- and S-fronts in Ω_s, and the interface Scholte wave propagating along Σ are all faithfully captured.

7 Conclusions

The key contribution of this work is an HDG method for the time-domain elasto-acoustic transmission problem built around a tailored penalty jump operator that encodes the inviscid slip condition at the fluid–solid interface, enabling a unified energy analysis of the coupled system without separate interface treatment. Well-posedness of the continuous problem is established via the Lumer–Phillips theorem, and optimal *hp*-error estimates for the semi-discrete scheme are proved in the energy norm. The stress-based formulation confers robustness in the nearly incompressible regime, as confirmed numerically. Temporal discretization is carried out with the second-order Crank–Nicolson method and L-stable SDIRK integrators for stiff regimes; convergence studies validate the theoretical rates and Ricker wavelet benchmarks against semi-analytical and HHO reference solutions confirm the accuracy of the method in configurations relevant to geophysics and biomedical imaging. Natural extensions include the derivation of improved L^2 velocity estimates for the velocity field via duality arguments and the coupling with poroelastic models for more realistic subsurface configurations.

A Finite element approximation properties

For any integer $m \geq 0$ and $K \in \mathcal{T}_h$, we denote by Π_K^m the $L^2(K)$-orthogonal projection onto $\mathcal{P}_m(K)$. This local projection extends naturally to a global projection $\Pi_{\mathcal{T}}^m : L^2(\mathcal{T}_h) \to \mathcal{P}_m(\mathcal{T}_h)$ by setting $(\Pi_{\mathcal{T}}^m v)|_K = \Pi_K^m(v|_K)$ for all $K \in \mathcal{T}_h$. Similarly, the global projection $\Pi_{\mathcal{F}}^m : L^2(\mathcal{F}_h) \to \mathcal{P}_m(\mathcal{F}_h)$ is given by $(\Pi_{\mathcal{F}}^m \widehat{v})|_F = \Pi_F^m(\widehat{v}|_F)$ for all $F \in \mathcal{F}_h$, where Π_F^m is the $L^2(F)$ orthogonal projection onto $\mathcal{P}_m(F)$. In the following, we maintain the notation $\Pi_{\mathcal{T}}^m$ to refer to the L^2-orthogonal projection onto $\mathcal{P}_m(\mathcal{T}_h, E)$, for $E \in \{\mathbb{R}^d, \mathbb{R}^{d\times d}_{\mathrm{sym}}\}$. When applied to tensor-valued functions, this projection preserves matrix symmetry as it acts component-wise. We start with a fundamental discrete trace inequality.

Lemma A.1. There exists a constant $C > 0$ independent of h and k such that

$$\|\tfrac{h_F^{1/2}}{k+1}\xi\|_{0,\partial\mathcal{T}_h} \leq C\|\xi\|_{0,\mathcal{T}_h} \quad \forall \xi \in \mathcal{P}_k(\mathcal{T}_h). \tag{A.1}$$

Proof. See [12, Lemma 3.2]. □

We employ the following two approximation error estimates as key ingredients in deriving our asymptotic *hp* error bounds.

LEMMA A.2. There exists a constant $C > 0$ independent of h and k such that

$$\|\xi - \Pi_{\mathcal{T}}^k \xi\|_{0,\mathcal{T}_h} + \|\tfrac{h_{\mathcal{F}}^{1/2}}{k+1}(\xi - \Pi_{\mathcal{T}}^k \xi)\|_{0,\partial\mathcal{T}_h} \leq C \tfrac{h_K^{\min\{r,k\}+1}}{(k+1)^{r+1}} \|\xi\|_{1+r,\Omega}, \tag{A.2}$$

for all $\xi \in H^{1+r}(\Omega)$, with $r \geq 0$.

Proof. See [12, Lemma 3.3]. □

LEMMA A.3 (Projection Error in Product Spaces). There exists a mesh- and polynomial degree-independent constant $C > 0$ such that for all $\boldsymbol{w} \in H^{2+r}(\Omega, \mathbb{R}^d)$ with $r \geq 0$:

$$\left| \left(\boldsymbol{w} - \Pi_{\mathcal{T}}^{k+1} \boldsymbol{w}, \boldsymbol{w}|_{\mathcal{F}_h} - \Pi_{\mathcal{F}}^{k+1}(\boldsymbol{w}|_{\mathcal{F}_h}) \right) \right|_{1,h} \leq C \tfrac{h^{\min\{r,k\}+1}}{(k+1)^{r+1/2}} \|\boldsymbol{w}\|_{2+r,\Omega}. \tag{A.3}$$

Proof. The result follows the proof technique of [12, Lemma 3.4]. □

B Time integration: SDIRK4

The semi-discrete HDG system (4.3) is a differential-algebraic system of index 1: the volume unknowns $(\boldsymbol{u}_h, \boldsymbol{\sigma}_{p,h})$ evolve in $\mathcal{H}_h^u \times \mathcal{H}_h^\sigma$, while $\widehat{\boldsymbol{u}}_h \in \mathcal{M}_h$ is determined algebraically at each instant by the constraint (5.2). We apply the 5-stage, order-4, L-stable SDIRK method of Hairer–Wanner [7, Sec. IV.6] with shared diagonal coefficient $\gamma = 1/4$. The common diagonal yields a single stage operator

$$\mathbf{P} = \frac{\mathbf{M}}{\gamma\, \Delta t} + \mathbf{S},$$

assembled and factorized once (via HDG static condensation on the mesh skeleton) and reused across all five stages and all time steps. Since $\mathbf{M}$ has a zero block for the facet component, the facet rows of each stage equation reduce to the algebraic constraint (5.2) evaluated at the stage time, so the facet unknowns are determined automatically without any special DAE treatment. The 5-stage SDIRK4 method of Hairer–Wanner [7, Sec. IV.6] has the Butcher tableau

$1/4$	$1/4$				
$3/4$	$1/2$	$1/4$			
$11/20$	$17/50$	$-1/25$	$1/4$		
$1/2$	$371/1360$	$-137/2720$	$15/544$	$1/4$	
1	$25/24$	$-49/48$	$125/16$	$-85/12$	$1/4$
	$25/24$	$-49/48$	$125/16$	$-85/12$	$1/4$

The method is L-stable and stiffly accurate. The shared diagonal coefficient $\gamma = 1/4$ allows a single factorization of the stage operator $\mathbf{P}$ to be reused across all five stages and all time steps. Although SDIRK4 has classical order 4, implicit Runge–Kutta methods applied to PDEs with time-dependent data are known to suffer order reduction [7]. In the particular setting of our stiff convergence study (Section 6.1), the effective temporal order saturates at 3 (see Figure 6.5).

References

[1] P.F. Antonietti, F. Bonaldi and I. Mazzieri, *A high-order discontinuous Galerkin approach to the elasto-acoustic problem*. Comput. Methods Appl. Mech. Engrg. 358 (2020), Paper No. 112634, 29 pp.

[2] B. Cockburn, J. Gopalakrishnan and R. Lazarov, *Unified hybridization of discontinuous Galerkin, mixed, and continuous Galerkin methods for second order elliptic problems*. SIAM J. Numer. Anal. 47 (2009), no. 2, 1319–1365.

[3] G. Cohen, *Higher-order numerical methods for transient wave equations*. J. Acoust. Soc. Am. 114 (2003), no. 1, 21–22.

[4] S. Du and F.-J. Sayas, *New analytical tools for HDG in elasticity, with applications to elastodynamics*. Math. Comp. 89 (2020), no. 324, 1745–1782.

[5] A. Ern and J.-L. Guermond, Finite elements III—first-order and time-dependent PDEs, volume 74 of Texts in Applied Mathematics. Springer, Cham, 2021.

[6] C. García, G.N. Gatica and S. Meddahi, *Finite element semidiscretization of a pressure–stress formulation for the time-domain fluid–structure interaction problem*. IMA J. Numer. Anal. 37 (2017), no. 4, 1772–1799. doi: 10.1093/imanum/drw079.

[7] E.Hairer and G. Wanner, Solving Ordinary Differential Equations II: Stiff and Differential-Algebraic Problems, volume 14 of Springer Series in Computational Mathematics. Springer-Verlag, Berlin, 2 edition, 1996.

[8] P.Houston, C. Schwab and E. Süli, *Discontinuous hp-finite element methods for advection-diffusion-reaction problems*. SIAM J. Numer. Anal. 39 (2002), no. 6, 2133–2163.

[9] D. Komatitsch and J.-P. Vilotte, *The spectral element method: an efficient tool to simulate the seismic response of 2D and 3D geological structures*. Bull. Seismol. Soc. Am. 88 (1998), no. 2, 368–392.

[10] J. Lysmer and R.L. Kuhlemeyer, *Finite dynamic model for infinite media*. J. Eng. Mech. Div. ASCE 95 (1969), 859–877.

[11] K.J. Marfurt, *Accuracy of finite-difference and finite-element modeling of the scalar and elastic wave equations*. Geophysics 49 (1984), no. 5, 533–549.

[12] S. Meddahi, *An hp error analysis of a hybrid discontinuous mixed Galerkin method for linear viscoelasticity*. Comput. Methods Appl. Mech. Engrg. 417 (2023), part A, Paper No. 116452, 18 pp.

[13] S. Meddahi, *An hp error analysis of HDG for linear fluid-structure interaction*. J. Sci. Comput. 102 (2025), no. 2, Paper No. 44, 34 pp.

[14] R. Mottier, A. Ern, R. Khot and L. Guillot, *Hybrid high-order methods for elasto-acoustic wave propagation in the time domain*. ESAIM Math. Model. Numer. Anal. 59 (2025), no. 5, 2685–2715. doi: 10.1051/m2an/2025062.

[15] N.C. Nguyen, J. Peraire and B. Cockburn, *High-order implicit hybridizable discontinuous Galerkin methods for acoustics and elastodynamics*. J. Comput. Phys. 230 (2011), no. 10, 3695–3718.

[16] J. Schöberl, C++ 11 *implementation of finite elements in ngsolve*. Institute for analysis and scientific computing, Vienna University of Technology, 30, 2014.

[17] J.P. Sheldon, S.T. Miller and J.S. Pitt, *A hybridizable discontinuous Galerkin method for modeling fluid-structure interaction*. J. Comput. Phys. 326 (2016), 91–114.

[18] S. Terrana, J.-P. Vilotte and L. Guillot, *A spectral hybridizable discontinuous Galerkin method for elastic–acoustic wave propagation*. Geophys. J. Int. 213 (2018), 574–602. doi: 10.1093/gji/ggx557.

[19] R. van Vossen, J.O.A. Robertsson and C.H. Chapman, *Finite-difference modeling of wave propagation in a fluid-solid configuration*. Geophysics 67 (2002), no. 2, 618–624.

Centro de Investigación en Ingeniería Matemática (CI^{2}MA)

PRE-PUBLICACIONES 2026

2026-09 Fahim Aslam, Zayd Hajjej, Jianghao Hao, Iqra Kanwal, Mauricio Sepúlveda, Rodrigo Véjar: *Stability and blow-up for a suspension bridge plate model with fractional damping and memory*

2026-10 Aníbal Coronel, Fernando Huancas, Mauricio Sepúlveda: *Identification of a power-like reaction term in a reaction-diffusion SIS model*

2026-11 Esteban Henriquez, Manuel Solano: *An unfitted HDG method for a distributed optimal convection-diffusion control problem*

2026-12 Sergio Caucao, Gabriel N. Gatica, Luis F. Gatica, Cristian Inzunza: *A priori and a posteriori error analysis of a mixed FEM for stationary convective Brinkman-Forchheimer flows with variable porosity*

2026-13 Jessika Camaño, Ricardo Oyarzúa, Katherine Rojo, Segundo Villa-Fuentes: *A mixed finite element method based on pseudostress and stream-function for the Navier–Stokes problem in 2D*

2026-14 Raimund Bürger, Cipriano Escalante, Enrique D. Fernández Nieto, Jorge Moya: *A two-dimensional multilayer shallow water model of tsunami-forest interaction*

2026-15 Alonso J. Bustos, Sergio Caucao: *A posteriori error analysis of two mixed formulations for a coupled Brinkman–Forchheimer and convection-diffusion-reaction system*

2026-16 Gabriel N. Gatica, Salim Meddahi, Kevin W. Pucha-Atan, Ricardo Ruiz-Baier: *A Banach spaces-based fully mixed finite element method for the thermo-electro-hydrodynamic Boussinesq problem*

2026-17 Tomás Barrios, Edwin Behrens, Rommel Bustinza, Jose M. Cascon: *A stabilized displacement - stress formulation for a linear elasticity problema with mixed boundary conditions*

2026-18 Gonzalo A. Benavides, Sergio Caucao, Gabriel N. Gatica, Yuri D. Sobral: *New Banach spaces-based mixed finite element methods for steady-state flows of magnetic fluids*

2026-19 Fahim Aslam, Marcelo Cavalcanti, Zayd Hajjej, You Haiyang Lin Bo, Mauricio Sepúlveda: *Blow-up of a Lamé system with fractional damping and infinite memory: theoretical and numerical study*

2026-20 Gabriel N. Gatica, Salim Meddahi: *A hybridizable discontinuous Galerkin method for the elasto–acoustic transmission problem*

Para obtener copias de las Pre-Publicaciones, escribir o llamar a: Director, Centro de Investigación en Ingeniería Matemática, Universidad de Concepción, Casilla 160-C, Concepción, Chile, Tel.: 41-2661324, o bien, visitar la página web del centro: `http://www.ci2ma.udec.cl`




Centro de Investigación en
Ingeniería Matemática (CI²MA)
Universidad de Concepción

Casilla 160-C, Concepción, Chile
Tel.: 56-41-2661324/2661554/2661316
http://www.ci2ma.udec.cl